Correlations and electronic order in a two-orbital honeycomb lattice model for twisted bilayer graphene

Jörn W. F. Venderbos[1,2] and Rafael M. Fernandes[3]

[1]*Department of Physics and Astronomy, University of Pennsylvania, Philadelphia, Pennsylvania 19104, USA*
[2]*Department of Chemistry, University of Pennsylvania, Philadelphia, Pennsylvania 19104, USA*
[3]*School of Physics and Astronomy, University of Minnesota, Minneapolis, Minnesota 55455, USA*

The recent observation of superconductivity in proximity to an insulating phase in twisted bilayer graphene (TBG) at small "magic" twist angles has been linked to the existence of nearly flat bands, which make TBG a fresh playground to investigate the interplay between correlations and superconductivity. The low-energy narrow bands were shown to be well described by an effective tight-binding model on the honeycomb lattice (the dual of the triangular Moiré superlattice) with a local orbital degree of freedom. In this paper, we perform a strong-coupling analysis of the proposed (p_x, p_y) two-orbital extended Hubbard model on the honeycomb lattice. By decomposing the interacting terms in the particle-particle and particle-hole channels, we classify the different possible superconducting, magnetic, and charge instabilities of the system. In the pairing case, we pay particular attention to the two-component (d-wave) pairing channels, which admit vestigial phases with nematic or chiral orders, and study their phenomenology. Furthermore, we explore the strong-coupling regime by obtaining a simplified spin-orbital exchange model which may describe a putative Mott-type insulating state at quarter-filling. Our mean-field solution reveals a rich intertwinement between ferromagnetic and antiferromagnetic orders with different types of nematic and magnetic orbital orders. Overall, our work provides a solid framework for further investigations of the phase diagram of the two-orbital extended Hubbard model in both strong- and weak-coupling regimes.

I. INTRODUCTION

The experimental discovery of superconductivity in twisted bilayer graphene (TBG) [1–3] has attracted much attention and has triggered a considerable theoretical effort to address this unexpected observation [4–48]. In particular, a renewed interest in the low-energy electronic properties of TBG structures has surfaced, geared towards incorporating correlations on the electronic structure via controlled approaches. From a more general perspective, the discovery of superconductivity on TBG has brought back into focus long-standing and much-debated questions concerning the interplay of electronic correlations and superconductivity [49–52].

Twisted bilayer graphene belongs to the class multilayer graphene systems generated by stacking sheets of monolayers. Given the large set of distinct stacking prescriptions, multilayer graphene systems offer a high degree of tunability of the resulting electronic structure [53,54]. By stacking two graphene sheets to form a bilayer and rotating ("twisting") one layer with respect to the other by an angle θ, one obtains a triangular Moiré superlattice structure (shown in Fig. 2) [55,56].

Based on an experimental study of TBG with small twist angles $\theta \sim 1°$, Cao *et al.* reported a metal-to-insulator transition at $T \approx 4$ K for carrier densities corresponding to $\pm 2e$ per Moiré supercell (with respect to charge neutrality) [1]. The conductance in the insulating state displays activated behavior with an activation energy $\Delta \approx 0.3$ meV, comparable to the metal-to-insulator transition temperature. Remarkably, upon

doping slightly away from $\pm 2e$ per supercell, either by adding holes or electrons, a superconducting state with a maximum transition temperature of $T_c \approx 1.7$ K was observed [2]. In fact, even the half-filled system was found to superconduct at low temperatures in the absence of a magnetic field for certain values of θ. The existence of superconductivity near an insulating state was also reported in Ref. [57], where pressure was used to tune the ground state of TBG with larger twist angles.

These observations raise important questions about the nature of the insulating and superconducting states, as well as the interplay between them. The fact that the insulating state appears at densities where single-particle considerations would predict metallic behavior hints at the importance of electronic correlations. Indeed, for twist angles $\theta \sim 1°$ numerical calculations had previously predicted the existence of Moiré minibands with almost flat dispersion near the Fermi level [58–61]. Some works reported a set of four narrow-bandwidth minibands (eight including spin degeneracy) separated from the other bands above and below [62,63], which appears to agree with the experimental findings. The small bandwidth $W \sim 10$ meV of this set of low-energy bands suggests that correlations are likely to provide the dominant energy scale and drive the system into a Mott-type state at quarter-filling.

On the other hand, the fact that the insulating transport behavior only onsets at relatively low temperatures comparable to T_c, combined with the small magnetic fields needed to kill the insulating state (of the order of 4 T), can be viewed as a challenge to the Mott-type scenario [10,12,23].

As a result, alternative explanations for the insulating state have been put forward [12,16,17,20,28,31,39]. Regardless of the microscopic origin of the insulating state, the onset of a relatively high-T_c state at its vicinity and at such low densities hint at the possibility of unconventional electronically driven pairing.

To answer these questions, appropriate models to describe the electronic structure are needed. Studies of TBG structures predating the recent experimental reports have addressed the electronic properties of TBG primarily within the framework of a low-energy continuum model, which starts from the Dirac electrons of the individual graphene layers [64–69]. This has proven to provide an excellent description for the low-energy electronic structure, in particular the appearance of nearly flat bands at charge neutrality, manifested by a vanishing of the Fermi velocity at special ("magic") twist angles. Since the manifold of nearly flat low-energy bands at charge neutrality is well separated from other bands, a description which accurately captures these bands may be sufficient.

Therefore, more recent works [5,6,14,18,19,21,34,40,43,44,48] have set out to formulate an effective tight-binding lattice model akin to (multiorbital) Hubbard models. The construction of an effective tight-binding model for the nearly flat bands, which relies on extracting localized Wannier states from the miniband structure, was shown to be contingent on the (exact and approximate) symmetries that are imposed on the model.[1] What is perhaps most important, however, is that any consistent formulation of a tight-binding model in terms of Wannier states was shown to require a honeycomb lattice structure [5,6]. Whereas the triangular Moiré lattice can be defined by regions of AA stacking, the dual honeycomb lattice is defined by regions of AB and BA stacking (see Fig. 2).

In this paper, we start from the extended two-orbital Hubbard model proposed in Refs. [5,18,21] and explore the effect of correlations on the low-energy flat bands. In this model, the orbitals have (p_x, p_y) symmetry and one of our main goals is to assess the role of the (p_x, p_y) orbital degrees of freedom on the superconducting, charge, and magnetic instabilities of the model. Here, we first decompose the interacting part of the Hubbard model, which involves both onsite and longer-range interactions, in the particle-particle and particle-hole channels. In this way, we obtain a general symmetry classification of pairing and particle-hole instabilities, which allows us to determine the effective interaction in each irreducible channel. The latter reveals which channels are most attractive (or least repulsive). In the case of pairing, we pay particular attention to the two-component (d-wave) superconductivity, which supports vestigial nonsuperconducting states with either chiral or nematic order. We argue that TBG is an ideal candidate to realize such vestigial states, given the reduced dimensionality of the system.

Having decomposed the interactions into irreducible channels, one can include the contributions from the kinetic term
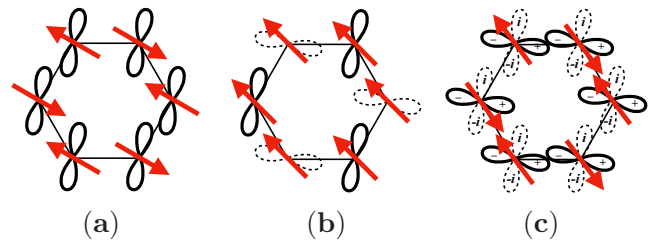

FIG. 1. Orbital and spin ordering. Schematic picture of the intertwined spin and orbital orderings appearing in the Mott insulating state at quarter-filling, as discussed in Sec. V. Solid and dashed orbitals refer to the different p_y and p_x orbitals. (a) Antiferromagnetic ferro-orbital order; (b) ferromagnetic antiferro-orbital order; (c) antiferromagnetic ferro-orbital-magnetic order with complex orbitals.

by either treating the kinetic part perturbatively (strong coupling) or the interaction terms perturbatively (weak coupling). In this paper, motivated by the small bandwidth of the low-energy flat bands, we explore the former regime, but we emphasize that the same formalism can also be used for weak-coupling analyses. Here, we focus on the putative Mott state at quarter-filling and consider an (anisotropic) spin-orbital exchange model, analogous to the Kugel-Khomskii–type Hamiltonians [70,71] commonly employed to describe strongly correlated multiorbital systems [72–75]. As a first step towards understanding the implications of such spin-orbital Hamiltonian, we perform a mean-field analysis in the case where only onsite interaction terms are kept. Depending of the ratio between the Hund's coupling J and the Hubbard U, we find antiferromagnetic order coupled either to a ferro-orbital nematic order or to a ferro-orbital magnetic order, or ferromagnetic order coupled to an SU(2) antiferro-orbital order. A schematic representation of these results is shown in Fig. 1.

As mentioned before, the Mott scenario should and will be subject to critical discourse. Insofar as the derivation and analysis of a spin-orbital exchange Hamiltonian is concerned, two important qualifying remarks are worth making. First, we note that in the derivation of such Hamiltonian only onsite repulsion is considered. In the context of TBG this is a rather restrictive assumption since the structure of the orbital Wannier states suggests that further-neighbor repulsion is non-negligible [21,23,28]. Second, the assumption of a small bandwidth W as compared to the (onsite) interaction energy scale U, i.e., $W/U \ll 1$, seems questionable given the small value of the activation transport gap Δ and the low temperature at which the metal-to-insulator transition takes place. Nevertheless, a careful examination of strong-coupling approaches to TBG are expected to offer interesting and important insight into the correlated physics of TBG.

The paper is organized as follows: Section II introduces and discusses the extended two-orbital Hubbard model with an emphasis on its symmetries. This section is largely a review of the studies which have proposed and constructed the two-orbital honeycomb lattice model, but we believe a thorough discussion may benefit the reader. In Secs. III and IV, the pairing instabilities and particle-hole instabilities

---

[1]A brief discussion of the intricacies involved in the Wannier state construction is given in Sec. II, with directions to the relevant references.
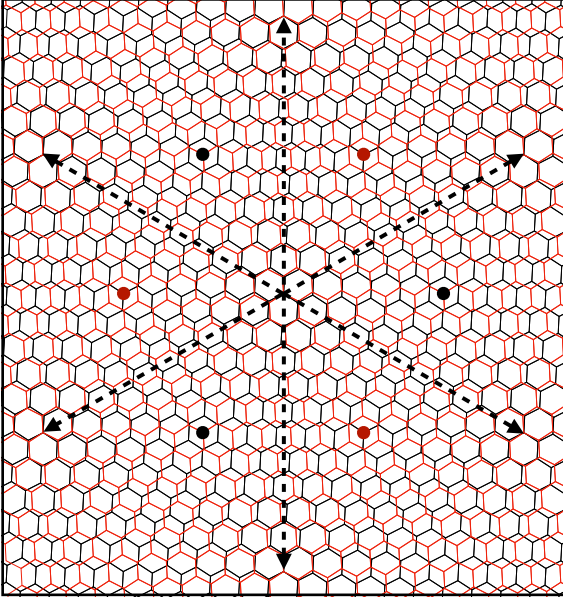
FIG. 2. Twisted bilayer graphene. Figure of two twisted graphene sheets, shown as black and red honeycomb nets, with commensurate Moiré superlattice periodicity. In this commensurate realization of twisted bilayer graphene, the twist angle is $\theta = 6.01°$ and the twist center is a pair of registered carbon atoms which defines the origin. The triangular superlattice vectors connecting regions of AA stacking are shown by dashed arrows. The black and red dots indicate the sites of the dual honeycomb (super)lattice and correspond to regions of AB and BA stacking, respectively.

are considered, respectively, by decomposing the interacting part of the Hamiltonian into irreducible superconducting and particle-hole channels. In Sec. V, the kinetic part is included perturbatively, and the resulting spin-orbital exchange model is derived and analyzed within a mean-field approach. Section VI is devoted to concluding remarks. A number of Appendices, Appendices A–F, collect additional details of the calculations presented in the main text.

II. LOW-ENERGY TWO-ORBITAL HUBBARD MODEL FOR TWISTED BILAYER GRAPHENE

A. General considerations

Our starting point is the effective extended Hubbard model for the low-energy flat bands of TBG developed in a series of recent works [5,6,18,21,34]. The effective tight-binding model for the flat-band manifold takes the form of a honeycomb lattice model with two Wannier orbitals per honeycomb lattice site, which was demonstrated based on a symmetry analysis [5] and an explicit calculation of maximally localized Wannier orbital wave functions [18,21]. The Bravais lattice vectors of the honeycomb lattice correspond to the lattice vectors of the triangular Moiré superlattice generated by the twist. The sites of the triangular Moiré superlattice can be identified with regions of local AA stacking, whereas the sublattices of the honeycomb lattice, which is the dual of the triangular lattice, mark the centers of local AB and BA stacking, respectively. This is shown in Fig. 2. Note that
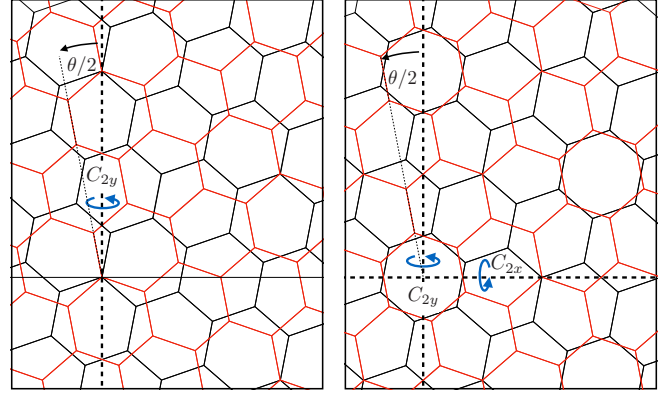

FIG. 3. Symmetry of TBG. (Left panel) Example of TBG structure with D_3 point-group symmetry. The twist rotation axis is coincident with a pair of registered carbon atoms. The structure has a twofold rotational symmetry C_{2y} about the y axis, and C_{3z} threefold rotational symmetry about the z axis. (Right) For comparison, we show a TBG structure where the twist rotation axis is coincident with the center of a hexagon, resulting in D_6 point-group symmetry. This implies an additional twofold rotational symmetry C_{2x}, and a C_{6z} sixfold rotational symmetry about the z axis. Both structures, left and right, have the same twist angle (and Moiré period), which was chosen large for illustrative purposes. Importantly, the twist center is also the center for the C_{3z} rotations, both for the D_3 and D_6 structures.

the structure of the honeycomb lattice implies four orbitals in the superlattice unit cell, i.e., two Wannier states per sublattice, which is consistent with the number of nearly flat bands forming the low-energy manifold. Importantly, in such a superlattice model the two Wannier orbitals transform in a specific way under spatial symmetries of TBG and these symmetry properties dictate the form of the hopping and interaction terms of the effective tight-binding model. For instance, in some cases the Wannier states were shown to transform as p-wave partners under rotations [5,18,21].

The construction of the honeycomb superlattice tight-binding model, and in particular the derivation of the localized Wannier functions, is predicated on two important assumptions, which are useful to state explicitly. The first assumption is the existence of exact lattice translation and point-group symmetries of TBG. The presence of exact translational symmetry of the twisted structure implies a commensurability condition on the Moiré supercell, which in turn implies a constraint on the twist angle θ. Note that for small but commensurate twist angles, the unit cell of the Moiré superlattice unit cell can become very large.

In addition to translational symmetry, the construction of the tight-binding model also assumes the existence of an exact point-group symmetry. Indeed, the aforementioned statement that the Wannier orbitals (in some cases) have p-wave symmetry can only have meaning when rotational symmetry is present. Commensurate TBG structures can belong to one of two possible dihedral point groups: D_3 or D_6. The difference in rotational symmetry depends on the center of twist rotation, as illustrated in Fig. 3. To understand this difference, consider starting from two AA stacked graphene sheets and rotating the top (bottom) layer by an angle $\theta/2$ ($-\theta/2$) about an axis

coincident with two registered carbon atoms, with θ defined with respect to the y axis. This results in a structure with threefold rotation symmetry C_{3z} along the z axis and twofold rotation symmetry C_{2y} along the y axis, as shown in the left panel of Fig. 3. Together these two symmetries generate D_3. The TBG structure shown in Fig. 2 is an example of the latter. Alternatively, if the twist rotation axis is coincident with the center of graphene hexagons, shown in the right panel of Fig. 3, the resulting TBG structure retains the sixfold C_{6z} rotation symmetry; in combination with C_{2y} this generates D_6 (which includes the twofold rotation C_{2x}).

A second important assumption of the Wannier orbital construction is the existence of an energy gap between the four flat bands and the other bands. The existence of such an energy gap has been predicted by theory [62,63] and appears to be consistent with experiment [1].

Following these considerations, we now introduce the honeycomb (super)lattice tight-binding model on which our study is based. The honeycomb lattice model we focus on in this work is meant to describe commensurate TBG structures with D_3 symmetry, shown in Fig. 3 on the left. It was shown that for this case the two Wannier orbitals at each superlattice site transform as two p-wave states [5,18,21]. This is a particularity of the D_3-symmetric structures, for which the center of the C_{3z} rotation is defined by registered carbon atoms [6,34]. In the case of commensurate structures with D_6 symmetry, the symmetry quantum numbers of the Wannier states were found to be different [6], resulting in a different tight-binding description of the low-energy flat bands. More generally, the construction of Wannier states depends on the exact and approximate symmetries of TBG which are imposed on the construction. Unless some (approximate) symmetries are ignored, the construction of localized symmetric Wannier states is obstructed [6,34]. Here, we do not give a full account of the subtleties and caveats related to construction of Wannier orbitals, in particular to the (exact or emergent) symmetries which are imposed, but instead refer the reader to the relevant Refs. [5,6,18,21,34,40], in particular Ref. [6].

B. Two-orbital extended Hubbard model

Given the symmetry of the Wannier states, we denote the orbitals at each site i as $p_{x,y}$ and define the corresponding electron annihilation (creation) operators as $c_{i\alpha\sigma}$ ($c_{i\alpha\sigma}^{\dagger}$) with $\alpha = x, y$ and $\sigma = \uparrow, \downarrow$ for spin. The kinetic part of the Hamiltonian describes the hopping processes and can be expressed as

$$H_K = \sum_{ij} c_i^{\dagger} \hat{T}(\mathbf{r}_{ij}) c_j + \text{H.c.}, \quad (1)$$

where $\hat{T}(\mathbf{r}_{ij})$ are hopping matrices and $\mathbf{r}_{ij} = \mathbf{r}_i - \mathbf{r}_j$ is the distance between sites i and j. Spin-orbit coupling is neglected, giving rise to full SU(2) spin rotational invariance.

For each set of bonds with fixed $\mathbf{r}_{ij}$ (i.e., nearest neighbors, next-nearest neighbors, etc.) the form of the hopping matrices is constrained by the transformation properties of the $p_{x,y}$ orbitals states under the D_3 point-group symmetry. Time-reversal symmetry imposes an additional constraint on the hopping matrices. A derivation of the symmetry constraints on the hopping matrices was presented in Ref. [18]; here, we
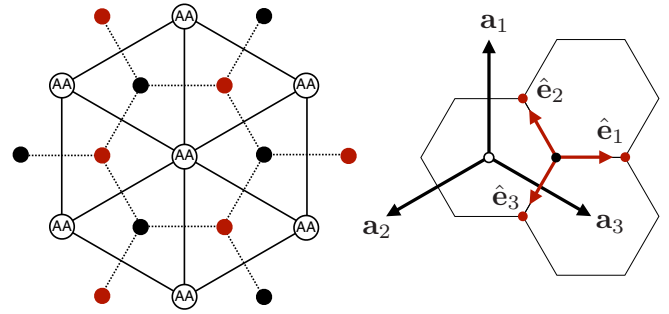

FIG. 4. Honeycomb superlattice model. (Left) Sketch of the effective honeycomb lattice extracted from twisted bilayer graphene with commensurate twist angle (see Fig. 2). The triangular Moiré superlattice, defined by the regions of AA stacking, is shown by solid lines. Red and black solid dots represent the sites of the honeycomb lattice (indicated by dashed lines), with different colors corresponding to the triangular sublattices of the honeycomb lattice. The sublattice sites coincide with regions of AB and BA stacking. (Right) Definition of lattice vectors. Here, $\mathbf{a}_{1,2,3}$ are lattice vectors of the (triangular) Moiré superlattice and $\hat{\mathbf{e}}_{1,2,3}$ are unit vectors corresponding to the directions of nearest-neighbor bonds.

review this briefly using a different formalism, with details given in Appendix B. To exploit rotational symmetry, we introduce a set of unit vectors corresponding to the bond directions; first, we define a general rotated frame

$$\hat{\mathbf{e}}_{\varphi} = \cos\varphi\,\hat{\mathbf{e}}_x + \sin\varphi\,\hat{\mathbf{e}}_y, \quad \hat{\mathbf{e}}_{\varphi}^{\perp} = -\sin\varphi\,\hat{\mathbf{e}}_x + \cos\varphi\,\hat{\mathbf{e}}_y, \quad (2)$$

where φ is an arbitrary angle and $\hat{\mathbf{e}}_{\varphi} \times \hat{\mathbf{e}}_{\varphi}^{\perp} = \hat{\mathbf{e}}_z$. The three nearest-neighbor unit vectors are then specified by $\varphi_n = 2\pi(n-1)/3$. We define the nearest-neighbor unit vectors as $\hat{\mathbf{e}}_{n=1,2,3}$ (see Fig. 4) and denote the corresponding hopping matrices as $\hat{T}_{n=1,2,3}^{(1)}$. Since the three hopping matrices are related by threefold rotations, only one needs to be specified. Focusing on $\hat{T}_1^{(1)}$, we find

$$\hat{T}_1^{(1)} = t_1 + t_1'\tau^z. \quad (3)$$

Here, the Pauli matrices $\tau^{x,y,z}$ act on the orbital degrees of freedom, i.e., $\tau^z = \pm 1$ corresponds to $p_{x,y}$. Note that the hopping matrix along the nearest-neighbor bond direction $\hat{\mathbf{e}}_{n=1}$ is diagonal in orbital space. By analogy with atomic p orbitals, we may introduce σ and π hopping processes as $t_{\sigma,\pi} = t_1 \pm t_1'$. The computation of $\hat{T}_{n=2,3}^{(1)}$ follows from (3) by appropriate rotations, as outlined in Appendices A and B.

Importantly, to reproduce details of the band structure of TBG, longer-ranged hopping processes must be included [5,18,21], in particular intrasublattice hopping matrices, i.e., hopping matrices connecting two sites on the same triangular sublattice. The most important hopping processes of this kind are second-nearest- and fifth-nearest-neighbor hopping. Viewed as bonds on the triangular sublattice, these are first-nearest and second-nearest-neighbor hoppings. We introduce the hopping matrices $\hat{T}_{n=1,2,3}^{(2)}$ and $\hat{T}_{n=1,2,3}^{(5)}$, with $\hat{T}_1^{(2)}$ in the direction of $\hat{\mathbf{e}}_y$ and $\hat{T}_1^{(5)}$ in the direction of $\hat{\mathbf{e}}_x$. (Note that the three second-nearest-neighbor bonds correspond to $\mathbf{a}_{1,2,3}$, as shown in Fig. 4.) Examining the constraints from symmetry,

we arrive at (see Appendix B)

$$\hat{T}_1^{(2)} = t_2 + t_{2z}\tau^z \pm t_{2x}\tau^x \pm it_{2y}\tau^y, \qquad (4)$$

$$\hat{T}_1^{(5)} = t_5 + t_{5z}\tau^z \pm t_{5x}\tau^x + it_{5y}\tau^y, \qquad (5)$$

where $+ (-)$ applies to the honeycomb sublattice A (B). As before, all other hopping matrices are obtained from rotation.

In principle, a symmetry analysis of this kind can be applied to any hopping process of arbitrary range, resulting in the most general form of Eq. (1) consistent with symmetry.

The relation of this two-orbital honeycomb lattice model to the underlying degrees of freedom of the individual graphene sheets (e.g., layer, sublattice, valley) deserves further discussion. We mentioned that the two sublattices of the Moiré honeycomb lattice, distinguished by black and red sites in Fig. 4, may be identified with regions of AB and BA stacking of the graphene layers, where A and B refer to the sublattice degree of freedom of each graphene sheet. There are thus two distinct notions of a sublattice degree of freedom, which should not be confused. Unless otherwise specified, in what follows the sublattice degree of freedom will be understood to refer to the emergent honeycomb superlattice.

More importantly, even though the two Wannier states have p-wave symmetry, which warrants the notation $p_{x,y}$, they should be clearly distinguished from physical atomic $p_{x,y}$ orbitals. This is evidenced by the fact that the hopping parameters of Eqs. (3)–(5), in particular the overlap integrals $t_{\sigma,\pi} = t_1 \pm t_1'$ of Eq. (3), are not determined by the Slater-Koster rules [76]. Indeed, application of the Slater-Koster rules would imply Hermitian hopping matrices. The hopping parameters can be directly calculated from the Wannier states, which were shown to have maxima at located at the AA stacking regions that form the triangular Moiré superlattice [18,21]. In particular, Ref. [21] demonstrated the following: (i) the Wannier states have spectral weight on both layers and both sublattices of each graphene layer; and (ii) the Wannier states can be associated with the valley degree of freedom of the constituent graphene layers [77]. This correspondence can be stated more precisely by forming the complex Wannier orbitals $p_\pm = p_x \pm ip_y$ and noting that, within the approach followed by Ref. [21], p_+ and p_- derive from valleys K and $K' = -K$, respectively. Furthermore, since the complex orbitals are eigenstates of τ^y, it is straightforward to see that if the hopping matrices of Eq. (1) [and in particular those of Eqs. (3)–(5)] only have nonzero terms proportional to the identity and τ^y, a larger internal U(1) symmetry in orbital space emerges, generated by τ^y.

By calculating the overlap between Wannier orbitals, both Refs. [18,21] found that this larger U(1) symmetry is a good approximate symmetry of the tight-binding model, although not exact. For Eq. (3), for instance, this implies $t_\sigma \approx t_\pi$ (i.e., $t_1' \ll t_1$). In addition, the importance of further-neighbor hopping terms was established, which can be traced back to the real-space extension of the Wannier states. We thus conclude that TBG with exact D_3 symmetry is well described by a kinetic tight-binding Hamiltonian (1) with longer-ranged hoppings and an approximate U(1) symmetry, which can be associated with the valley quantum number. We note in passing that for a rather different set of parameters, i.e.,

only nearest-neighbor σ hopping ($t_1' = t_1$), the physics of the honeycomb lattice p-orbital model was shown to give rise to interesting physics, albeit most likely not relevant to TBG [78,79].

Next, we consider the interacting part of the Hamiltonian H_I. The interacting Hamiltonian may be viewed as a sum of two types of terms: density-density interaction terms and exchange terms. In its most general form, H_I is given by

$$
\begin{aligned}
H_I = & \frac{1}{2}\sum_{ij} V_{ij}^{\alpha\beta} n_{i\alpha} n_{j\beta} + \frac{1}{2}\sum_{ij,\alpha\beta} J_{1,ij}^{\alpha\beta} c_{i\alpha\sigma}^\dagger c_{j\beta\sigma'}^\dagger c_{i\beta\sigma'} c_{j\alpha\sigma} \\
& + \frac{1}{2}\sum_{ij,\alpha\neq\beta} J_{2,ij}^{\alpha\beta} c_{i\alpha\sigma}^\dagger c_{j\beta\sigma'}^\dagger c_{i\alpha\sigma'} c_{j\beta\sigma} \\
& + \frac{1}{2}\sum_{ij,\alpha\neq\beta} J_{3,ij}^{\alpha\beta} c_{i\alpha\sigma}^\dagger c_{j\alpha\sigma'}^\dagger c_{i\beta\sigma'} c_{j\beta\sigma},
\end{aligned} \qquad (6)
$$

where the first term describes density-density interactions and the remaining three terms describe exchange interactions. The four sets of interaction parameters are not fully independent, but must satisfy the constraint of invariance under rotations in orbital space (for a formulation of this constraint, see Appendix C). For each set of the interaction parameters we furthermore assume $V_{ij}^{xy} = V_{ij}^{yx}$ and $V_{ij}^{xx} = V_{ij}^{yy}$, and similarly for $J_{1,2,3}$. Finally, we note that the interaction parameters are invariant under translations $V_{ij}^{\alpha\beta} \equiv V^{\alpha\beta}(\mathbf{r}_i - \mathbf{r}_j)$, and similarly for the exchange terms.

An extended Hubbard model of the form of Eq. (6) was proposed in Ref. [21], where the interaction parameters were estimated using the Coulomb interaction and the explicit wave functions of the Wannier states. Such estimates showed that further-neighbor interactions, while smaller than onsite interactions, are non-negligible. In addition, in the context of the model used in Ref. [21] the exchange interactions $J_{2,3}$ were found to be considerably smaller than J_1. In Secs. III and IV, where we study the pairing and particle-hole instabilities, we consider H_I in its general form of Eq. (6). The main physical motivation to do so is that, because (6) is meant to describe the effective interactions within the manifold of the low-energy flat bands, they are expected to get renormalized by integrating out higher-energy degrees of freedom (see, for instance, Ref. [80]).

In Sec. V, where we focus on the strong-coupling regime, we study a particular limiting case of H_I and only consider the onsite interactions. Despite the fact that further-neighbor interactions may not be too much smaller than the onsite terms, this approximation is useful as it allows for the derivation of a spin-orbital exchange Hamiltonian. Keeping onsite interactions only ($i = j$) in Eq. (6), the parameters $J_{1,ii}^{\alpha\beta}$ are equivalent to $V_{ii}^{\alpha\beta}$, and the former may thus be set to zero. The remaining interaction parameters can be specified in terms of two interaction energy scales: a Hubbard interaction U and a Hund's rule coupling J [5]. In terms of these two parameters, the nonzero onsite interaction coefficients of Eq. (6) are $V^{xx} = V^{yy} = U$, $V^{xy} = V^{yx} = U - 2J$, and $J_{2,3}^{xy} = J_{2,3}^{yx} = J$. As a result, the Hamiltonian H_I acquires the

standard Hubbard-Kanamori form [81]

$$H_I^{(\text{onsite})} = U \sum_{i,\alpha} n_{i\alpha\uparrow} n_{i\alpha\downarrow} + (U - 2J) \sum_i n_{ix} n_{iy}$$

$$+ J \sum_{i,\sigma,\sigma'} c_{ix\sigma}^\dagger c_{iy\sigma'}^\dagger c_{ix\sigma'} c_{iy\sigma}$$

$$+ J \sum_{i,\alpha\neq\beta} c_{i\alpha\uparrow}^\dagger c_{i\alpha\downarrow}^\dagger c_{i\beta\downarrow} c_{i\beta\uparrow}. \tag{7}$$

Having derived the full interacting model, in the next sections we discuss and classify the different instabilities of the model. By directly decomposing the interacting term H_I into different irreducible channels, we obtain the effective interactions corresponding to the possible instabilities in the particle-particle (i.e., superconducting) and particle-hole channels in Secs. III and IV, respectively. In Sec. V, we go one step beyond and, in the spirit of the strong-coupling approach, include perturbatively the kinetic Hamiltonian H_K, deriving the low-energy spin-orbital exchange model.

III. SUPERCONDUCTING INSTABILITIES AND THEIR VESTIGIAL ORDERS

In this section we focus attention on the interacting Hamiltonian H_I of Eq. (6) and address the question of superconductivity. In particular, we analyze the pairing instabilities of H_I by decomposing the interaction into irreducible pairing channels. The symmetry group of the normal state allows for a two-component d-wave pairing channel, which gives rise to the interesting possibility of chiral or nematic d-wave superconductivity. This possibility is studied in more detail in Sec. III B.

A. Decomposition of the interaction

To decompose the interaction into irreducible pairing vertices, we first identify the symmetry of the Cooper pairs. The full symmetry group of the normal state, including spin rotational symmetry, is $\mathcal{G} = D_3 \otimes \text{SO}(3)$ (note that here we restrict to the exact point-group symmetries of TBG). This implies that the pairing channels are labeled by the spin angular momentum S of the Cooper pair, which can take the values $S = 0, 1$, and the representations Γ of D_3, which can take the values $E \otimes E = A_1 \oplus A_2 \oplus E$ associated with the product of two orbitals. The decomposition of the representation product describes the possible orbital structure of the Cooper pair.

To proceed, we define the pair creation operator $\Pi_{i\alpha\sigma, j\beta\sigma'}^\dagger$:

$$\Pi_{i\alpha\sigma, j\beta\sigma'}^\dagger = c_{i\alpha\sigma}^\dagger c_{j\beta\sigma'}^\dagger, \tag{8}$$

A general pairing operator of this form can be decomposed into irreducible pairing operators defined by the symmetry quantum numbers (Γ, S, M). Here, Γ denotes the point-group representation and $S = 0, 1$ distinguishes spin-singlet and spin-triplet pairing: $M = -S, \ldots, S$. This decomposition is given by

$$\Pi_{i\alpha\sigma, j\beta\sigma'}^\dagger = \sum_\Gamma \sum_{S,M} X_{\alpha\beta}^\Gamma C_{\sigma\sigma'}^{SM} \Pi_{ij,\Gamma,SM}^\dagger, \tag{9}$$

where $C_{\sigma\sigma'}^{SM}$ are the appropriate Clebsch-Gordan coefficients and $X_{\alpha\beta}^\Gamma$ are the analogs of Clebsch-Gordan coefficients for the orbital sector. The expressions for the latter are provided in Appendix C. Note that here the sum over Γ includes a sum over the individual components of multidimensional representations, which we leave implicit for the benefit of a more compact notation (the latter is important and the reader is cautioned to keep this is mind).

To see how this leads to a decomposition into irreducible pairing terms, consider the first term of H_I [Eq. (6)], with interaction parameters $V_{ij}^{\alpha\beta}$. Substituting Eq. (9) and taking sums we arrive at

$$H_I = \frac{1}{2} \sum_{ij} \sum_{SM} \sum_\Gamma V_{ij}^\Gamma \Pi_{ij,\Gamma,SM}^\dagger \Pi_{ij,\Gamma,SM}, \tag{10}$$

with interaction parameters V_{ij}^Γ given by

$$V_{ij}^\Gamma = \sum_{\alpha\beta} X_{\alpha\beta}^\Gamma V_{ij}^{\alpha\beta} X_{\alpha\beta}^\Gamma. \tag{11}$$

The Hamiltonian of Eq. (10) is diagonal in the space defined by the spin and orbital quantum numbers (S, M) and Γ. It should be noted, however, that the interaction parameters V_{ij}^Γ need not be the same for different components of the same (multidimensional) representation (recall that the sum over Γ implies a sum over its components). This is not inconsistent with the notion of irreducible coupling constants since these can only be defined for the full Hamiltonian H_I. The latter includes the interaction terms $J_{1,2,3}$; substituting the decomposition of Eq. (9) into these remaining terms of H_I leads to similar expressions as Eq. (10), which can be combined to yield (details are presented in Appendix C)

$$H_I = \frac{1}{2} \sum_{ij} \sum_{SM} \sum_\Gamma U_{ij}^\Gamma \Pi_{ij,\Gamma,SM}^\dagger \Pi_{ij,\Gamma,SM}. \tag{12}$$

The matrix elements U_{ij}^Γ are given by the appropriate sums of V and $J_{1,2,3}$, and define the irreducible coupling constants associated with the representation Γ.

Fermi statistics put restrictions on the allowed combinations of Γ and S. This is apparent when $i = j$, in which case spin-singlet pairing ($S = 0$) can only occur for the even representations A_1 and E, whereas spin-triplet pairing ($S = 1$) can only have A_2 symmetry. In general, the combination of Γ and S determines whether $\Pi_{ij,\Gamma,SM}^\dagger$ is even or odd under the exchange $i \leftrightarrow j$.

To illustrate the application of Eq. (12), consider the case in which the interaction terms of Eq. (6) are only onsite, giving rise to Eq. (7). We can express the resulting onsite pair creation operators in the following more familiar form:

$$\Pi_\Gamma^\dagger = c_{i\alpha\sigma}^\dagger [\hat\Delta_\Gamma (is^y)]_{\alpha\beta}^{\sigma\sigma'} c_{i\beta\sigma'}^\dagger, \quad \hat\Delta_\Gamma = (\Delta_\Gamma)_{ab} \tau^a s^b, \tag{13}$$

where $\hat\Delta_\Gamma$ is a matrix in orbital and spin space, which is expanded in two sets of Pauli matrices τ^a and s^b ($a, b = 0, x, y, z$). Here, τ^0 and s^0 are defined as the identity. As before, $\tau^z = \pm 1$ labels the orbital degree of freedom and $s^z = \pm 1$ corresponds to spin $\uparrow, \downarrow$. Note that we included explicitly the antisymmetric tensor in spin space $(is^y)_{\alpha\beta} = \epsilon_{\alpha\beta}$. As mentioned, due to Fermi statistics, which can be expressed as $s^y \hat\Delta_\Gamma^T s^y = \hat\Delta_\Gamma$, there are three distinct onsite pairing channels,

TABLE I. Effective interactions for the three different types of onsite particle-particle (superconducting) orders.

U^Γ	$\Gamma = A_1$	$\Gamma = A_2$	$\Gamma = E_2$
Singlet	$U + J$		$U - J$
Triplet		$U - 3J$	

which are uniquely labeled by the three representations A_1, A_2, and E.

The onsite pair operators with A_1 and E_2 symmetry are spin-singlet orbital-triplet states and represented by the matrices

$$\hat{\Delta}_{A_1} = 1, \tag{14}$$

$$\hat{\Delta}_E = (\tau^z, \tau^x). \tag{15}$$

Here, the second equality expresses the fact that E_2 is two-component representation. The pair operators with A_2 symmetry form a (orbital-singlet) spin-triplet state transforming as SO(3) under rotations in spin space and are expressed as

$$\hat{\Delta}_{A_2} = \tau^y(s^x, s^y, s^z). \tag{16}$$

Written in this form, the pairing operators are not normalized. To normalize them we multiply all matrices $\hat{\Delta}_\Gamma$ as written in Eqs. (14) and (16) by a factor $1/2\sqrt{2}$ [82].

The coupling constants $U^\Gamma = U_{ii}^\Gamma$ of the onsite pairing vertices, defined in Eq. (12), can then be obtained in a straightforward way. For onsite interactions [Eq. (7)], one finds the effective interactions U^Γ of the three onsite pairings described above as (see also Table I):

$$U^{A_1} = U + J, \quad U^{A_2} = U - 3J, \quad U^E = U - J. \tag{17}$$

Note that the factor $\frac{1}{2}$ in (12) was absorbed in the normalization of the onsite pairing operators (see [82]). Although a full analysis of the leading superconducting instabilities is beyond the scope of this work, it is interesting to note that the "Hund's rule" coupling J favors the A_2 and E states.

To proceed with the general analysis of Eq. (12), it is convenient to go to momentum space by Fourier transforming the pair creation operators. Specifically, we define

$$\Pi_{ij}^\dagger = \frac{1}{N} \sum_\mathbf{k} \Pi_{\mathbf{k}\nu_i\nu_j}^\dagger e^{i\mathbf{k}\cdot(\mathbf{r}_i - \mathbf{r}_j)}, \tag{18}$$

where $\Pi_{\mathbf{k}\nu_i\nu_j}^\dagger = c_{\mathbf{k}\nu_i}^\dagger c_{-\mathbf{k}\nu_j}^\dagger$ and $\nu_{i,j} = A, B$ refers to the sublattice degree of freedom of the honeycomb superlattice, and N is the system size. In Eq. (18), spin and orbital indices have been suppressed for simplicity. Substituting the Fourier transform into (12), one finds (suppressing the spin label S)

$$H_I = \frac{1}{N} \sum_{\mathbf{k}\mathbf{k}'} \sum_\Gamma \sum_{\nu\nu'} U_{\nu\nu'}^\Gamma(\mathbf{k}' - \mathbf{k}) \Pi_{\mathbf{k}\nu\nu',\Gamma}^\dagger \Pi_{\mathbf{k}'\nu\nu',\Gamma}, \tag{19}$$

where the momentum-dependent effective interaction $U_{\nu\nu'}^\Gamma(\mathbf{k})$ is given by

$$U_{\nu\nu'}^\Gamma(\mathbf{k}) = \sum_{\mathbf{r}_{ij}} U_{ij}^\Gamma e^{-i\mathbf{k}\cdot\mathbf{r}_{ij}}. \tag{20}$$

This effective interaction may be compared to those of more familiar single-band models, or of an isotropic continuum model for a Fermi surface. Such effective interactions typically originate from (some form of) density-density interaction. Here, apart from an additional label Γ associated with the orbital degree of freedom, the effective interaction has a similar structure. In particular, as is clear from Eq. (20), it is the Fourier transform of (short-ranged) interactions between first-, second-, and further-nearest-neighbor pairs, each with their own interaction parameter.

The standard next step is to decompose $U_{\nu\nu'}^\Gamma(\mathbf{k}' - \mathbf{k})$ into a sum over harmonics, in this case (honeycomb) lattice harmonics, which are labeled by the symmetry quantum numbers of the lattice, i.e., the point-group representations. Such decomposition is based on the fact that a general function $g(\mathbf{k})$ which has the symmetry of the lattice can be expanded as $g(\mathbf{k}' - \mathbf{k}) = \sum_{\Gamma'} f^{\Gamma'*}(\mathbf{k}') f^{\Gamma'}(\mathbf{k})$, where $f^{\Gamma'}(\mathbf{k})$ are the lattice harmonics which transform irreducibly.[2] Lattice harmonics are the lattice equivalents of spherical harmonics in isotropic systems; the latter are labeled by angular momentum quantum numbers. An important difference with respect to isotropic systems is the finite set of lattice symmetry quantum numbers, which implies that distinct harmonics fall into the same channel. Once the effective interaction (20) is decomposed into lattice harmonics, the harmonics labeled by Γ' are combined with the corresponding pairing operators labeled by Γ (referring to the orbitals) to form the products $\Gamma' \otimes \Gamma$, which are reducible. Decomposition of the product representation then yields pairing operators fully symmetrized with respect to the symmetry group of the system. Here, we do not work this out in detail, but refer the reader to Appendix D for a more detailed discussion of decomposing (20), as well as Ref. [83]. Instead, we briefly showcase the trivial case of onsite pairing in the context of Eqs. (19) and (20).

The onsite component of $U_{\nu\nu'}^\Gamma(\mathbf{k})$ is simply given by $U_{AA,0}^\Gamma = U_{BB,0}^\Gamma \equiv U_0^\Gamma$. What remains to be done is to symmetrize the pairing operators with respect to the honeycomb sublattice degree of freedom. To this end, we define the even and odd linear combinations

$$\Pi_{\mathbf{k}AA,\Gamma}^\dagger + \Pi_{\mathbf{k}BB,\Gamma}^\dagger = \sum_{\nu\nu'} \delta_{\nu\nu'} \Pi_{\mathbf{k}\nu\nu',\Gamma}^\dagger, \tag{21}$$

$$\Pi_{\mathbf{k}AA,\Gamma}^\dagger - \Pi_{\mathbf{k}BB,\Gamma}^\dagger = \sum_{\nu\nu'} \sigma_{\nu\nu'}^z \Pi_{\mathbf{k}\nu\nu',\Gamma}^\dagger, \tag{22}$$

where $\sigma^z = \pm 1$ is an A, B sublattice label. The former is fully symmetric, whereas the latter is odd under C_{2y}.

At this stage it is useful to briefly connect to the recent theoretical work on superconductivity in TBG. A number of works have addressed the question of pairing in TBG [4,7,8,13,15,16,20,22,24–26,29,30,35–38,47], using different methods (numerical and analytical) as well as different models. For the sake of simplicity, some authors have considered a (two-orbital) triangular lattice model or have considered the SU(4) symmetric limit of the honeycomb lattice model. Approaches have also differed in the type of interactions

---

[2]As before, the sum over representations Γ' includes an implicit sum over components of multidimensional representations.

included. Furthermore, while most works focused on super-conductivity from repulsive interactions, others have explored phonon-mediated scenarios in more detail [22,37].

Here, we have presented a full symmetry-based decomposition of the extended Hubbard interaction (6) into pairing channels and have obtained the corresponding coupling constants. Our starting point is the two-orbital honeycomb lattice model, for which we do not assume artificial higher symmetry. Notably, we make no *a priori* assumptions on the range of the included interaction; the interacting Hamiltonian (19) is fully general. As a result, (19) provides the basis for studying the pairing instabilities using various schemes. For instance, the renormalization of the interactions by particle-hole fluctuations, treated within random phase approximations (RPA), can be straightforwardly included [16]. To this end, we derive the corresponding decomposition in particle-hole channels in Sec. IV.

B. Two-component pairing and vestigial ordering

The existence of a two-component pairing channel, which is guaranteed when the normal state has D_3 symmetry, merits a more detailed discussion of the consequences of two-component superconductivity in TBG. Since superconductors described by a two-component order parameter break additional symmetries of the system, such as time-reversal or rotational symmetry, they exhibit distinct signatures in experimental probes which may be used to establish the pairing symmetry. With this in mind we focus attention on the two-component superconducting channel with symmetry label E (hereafter denoted E pairing) and consider its phenomenology in the context of TBG. It is natural to refer to this two-component pairing channel as d-wave pairing; superconductivity with this pairing symmetry has been the focus of a number of recent studies addressing superconductivity in TBG [4,8,13,16,20,29,30,36,47].

To describe an E-pairing state, it is necessary to introduce a two-component complex order parameter (η_1, η_2) which transforms as the E representation of the D_3 group. The possible superconducting ground states can be obtained by analyzing the Ginzburg-Landau expansion of the free energy in terms of the superconducting order parameter [84]:

$$F = r(|\eta_1|^2 + |\eta_2|^2) + u(|\eta_1|^2 + |\eta_2|^2)^2 + v|\eta_1^*\eta_2 - \eta_2^*\eta_1|^2. \tag{23}$$

Here, $r \propto T - T_c$, where T_c is the transition temperature, and u, v are fourth-order expansion coefficients. The state realized below T_c ($r < 0$) is determined by the fourth-order interaction v. When $v < 0$, the superconducting ground state is chiral, i.e., time-reversal symmetry breaking (TRSB), and given by $(\eta_1, \eta_2) = \eta_0(1, \pm i)$. Here, η_0 is a complex number. A number of recent theoretical studies have argued that this chiral d-wave state is favored in TBG [8,13,16,20,29,30,47]. On the other hand, when $v > 0$, the superconducting ground state is given by $(\eta_1, \eta_2) = \eta_0(\cos\phi, \sin\phi)$. Since it preserves time-reversal symmetry but lowers the point-group symmetry, in particular threefold rotations, it is a nematic superconductor [85,86]. Importantly, the values of ϕ are restricted due to the crystal symmetries. This can be seen by considering the

following sixth-order term in the free-energy expansion:

$$F^{(6)} = \frac{\lambda}{2}[(\eta_1 - i\eta_2)^3(\eta_1^* - i\eta_2^*)^3 + \text{c.c.}]. \tag{24}$$

For the TRSB superconducting state, this term vanishes. For the nematic superconducting state, however, this term becomes $\lambda|\eta_0|^6\cos 6\phi$, which is minimized either by $\phi = n\pi/3$ (for $\lambda < 0$) or $\phi = (n + \frac{1}{2})\pi/3$ (for $\lambda > 0$), with integer n.

The existence of a multicomponent superconducting order parameter opens the possibility of vestigial order, i.e., the condensation of bilinear combinations of η_i that break certain symmetries of the lattice while preserving the U(1) superconducting gauge symmetry (for a review, see [87,88]). Importantly, these bilinear combinations may condense even in the nonsuperconducting state, giving rise to an ordered state that precedes the onset of superconducting order. In the case of TBG, since it is a two-dimensional system, superconducting phase fluctuations are very strong and melt long-range superconducting order completely. However, the phase with composite bilinear order is not affected by these strong fluctuations since it is associated with a discrete symmetry, and thus remains as a vestige of the superconducting state.

Following Ref. [87] and the analysis of the nematic p-wave superconductor of Ref. [89], we identify two possible vestigial orders, associated with the TRSB and nematic superconducting states. In the case of a TRSB superconductor, the composite order parameter with chiral symmetry is given by

$$\psi = i(\eta_1\eta_2^* - \eta_2\eta_1^*) \equiv \boldsymbol{\eta}^\dagger\sigma^y\boldsymbol{\eta}, \tag{25}$$

where $\boldsymbol{\eta} = (\eta_1, \eta_2)^T$ and σ^y is a Pauli matrix. It is clear that ψ is a Z_2 Ising-type order parameter, whose condensation implies TRSB (chiral order). Therefore, the vestigial state with $\langle\psi\rangle \neq 0$ but $\langle\boldsymbol{\eta}\rangle = 0$, which is expected to take place at finite temperatures in two dimensions, is a nonsuperconducting state that breaks time-reversal symmetry.

In the case of the nematic superconductor, the composite order parameter describing nematic order has two components, which transform as partners of the two-dimensional irreducible representation E:

$$(\Psi_1, \Psi_2) = (|\eta_1|^2 - |\eta_2|^2, \eta_2^*\eta_1 + \eta_1^*\eta_2),$$

$$\boldsymbol{\Psi} \equiv (\boldsymbol{\eta}^\dagger\sigma^z\boldsymbol{\eta}, \boldsymbol{\eta}^\dagger\sigma^x\boldsymbol{\eta}). \tag{26}$$

Since $\boldsymbol{\Psi}$ is a composite order parameter and $\boldsymbol{\Psi} \propto (\cos 2\phi, \sin 2\phi)$ for $(\eta_1, \eta_2) = \eta_0(\cos\phi, \sin\phi)$, it is natural to think of it as a $\mathbf{q} = 0$ particle-hole order parameter with d-wave symmetry, whose two components transform as $d_{x^2-y^2}$ and d_{xy}, It should be kept in mind, however, that the symmetries of D_3 do not distinguish p and d waves. Importantly, the condensation of $\boldsymbol{\Psi}$ implies that the system is no longer invariant under an in-plane C_{3z} rotation and in this sense the ordered state can be called nematic. As a result, the vestigial phase with $\langle\boldsymbol{\Psi}\rangle \neq 0$ but $\langle\boldsymbol{\eta}\rangle = 0$ defines a nematic phase.

At first sight, one might be tempted to identify $\boldsymbol{\Psi}$ with an XY nematic order parameter, which would not order at finite temperatures in two dimensions due to Mermin-Wagner theorem. However, due to crystal anisotropy $\boldsymbol{\Psi}$ is actually a Z_3 order parameter and falls in the same universality class as the three-state Potts model [89,90]. Note that this distinguishes it from a Z_2 Ising nematic order parameter. Indeed, writing the

Landau free-energy expansion for $\boldsymbol{\Psi}$ reveals the existence of a cubic term:

$$F_\Psi = r'\left(\Psi_1^2 + \Psi_2^2\right) + \lambda'\left(\Psi_+^3 + \Psi_-^3\right) + u'\left(\Psi_1^2 + \Psi_2^2\right)^2, \quad (27)$$

where $\Psi_\pm = \Psi_1 \pm i\Psi_2$. Note that the existence of a cubic term is implied by the presence of the sixth-order term (24); in particular, substituting (26) into the cubic term of (27) gives (24).

Writing $\Psi_+ = |\Psi|e^{i\theta}$ and expressing the cubic term in terms of the phase θ gives $2\lambda'|\Psi|^3 \cos 3\theta$. For $\lambda' < 0$ the set of degenerate minima is given by $\theta = 2n\pi/3$ with n integer; for $\lambda' > 0$, it is given by $\theta = (2n+1)\pi/3$. Thus, because θ can assume three different values, $\boldsymbol{\Psi}$ is a discrete Z_3 order parameter, which can condense at finite temperatures in two dimensions. As a result, a vestigial nematic order is possible to be realized in TBG. Note that the presence of the cubic order term makes the nematic transition first order within mean-field theory [89]. However, in two dimensions, which is the case relevant for TBG, fluctuations drive the Z_3 transition second order, with a small critical exponent β for the order parameter $\beta = \frac{1}{9}$ [90]. The small value of β indicates a steep onset of the nematic order parameter, which may in some experiments be similar to a jump. Furthermore, the allowed θ values correspond to the $\pm d_{x^2-y^2}$ nematic state ($\theta = 0$ and π, respectively), or to the symmetry-equivalent states related to $\pm d_{x^2-y^2}$ by threefold rotations. As a result, the d_{xy} nematic state ($\theta = \pm\pi/2$) is never realized, as it is never a minimum of the free energy.

IV. PARTICLE-HOLE INSTABILITIES

In Sec. III A, for the purpose of studying superconductivity, we decomposed the interactions into irreducible pairing (particle-particle) channels. A similar approach can be taken to study instabilities towards particle-hole order, such as magnetic, charge, or orbital order. Therefore, in this section we present a decomposition of Eq. (6) into irreducible particle-hole channels. We begin by defining the general particle-hole operators $\Lambda_{i\alpha\sigma,j\beta\sigma'}$ as

$$\Lambda_{i\alpha\sigma,j\beta\sigma'} = c_{i\alpha\sigma}^\dagger c_{j\beta\sigma'}, \quad (28)$$

which are the analogs of Eq. (8). In a manner similar to Eq. (9) we decompose these operators into irreducible particle-hole operators $\Lambda_{ij,\Gamma a}$ as

$$\Lambda_{i\alpha\sigma,j\beta\sigma'} = \sum_\Gamma \sum_a Y_{\alpha\beta}^\Gamma \widetilde{C}_{\sigma\sigma'}^a \Lambda_{ij,\Gamma a}, \quad (29)$$

where $a = 0, x, y, z$ is an index for spin-singlet ($a = 0$) and spin-triplet ($a = x, y, z$) particle-hole condensates. Here, the singlet and triplet operators are defined as $\Lambda_{ij,a} = \sum_{\sigma\sigma'} c_{i\sigma}^\dagger s_{\sigma\sigma'}^a c_{j\sigma'}$, where $s^{x,y,z}$ are the spin Pauli matrices and s^0 is the identity. The irreducible orbital operators $\Lambda_{ij,\Gamma}$ are defined similarly; the expansion coefficients $Y_{\alpha\beta}^\Gamma$ and $\widetilde{C}_{\sigma\sigma'}^a$, which can be related to Clebsch-Gordan coefficients, are provided in Appendix E. Note that the relation $\Lambda_{ij,\Gamma a}^\dagger = \Lambda_{ji,\Gamma a}$ holds.

Equation (29) is the equivalent of (9). As a first step towards decomposing the interaction into particle-hole channels, we thus proceed similarly by substituting (29) into H_I.

TABLE II. Effective interactions for onsite particle-hole order, defined by Eq. (32), in terms of the interaction parameters U and J defined in Eq. (7). Six different channels can be distinguished based on the spin (i.e., singlet or triplet) and orbital structure of the particle-hole channel.

Onsite $\tilde{U}^{\Gamma a}$	$\Gamma = A_1$	$\Gamma = A_2$	$\Gamma = E$
Singlet	$(3U - 5J)/8$	$(J - U)/8$	$(5J - U)/8$
Triplet	$-(U + J)/8$	$(J - U)/8$	$(J - U)/8$

As in the case of the pairing channels [Eq. (10)], we initially illustrate this procedure by using the density-density terms with interaction parameters V. In the present case, contrary to the pairing decomposition, we expect to obtain two terms, as there are two ways to form particle-hole bilinears. We find for the interaction H_V,

$$H_V = \frac{1}{2} \sum_{ij} \sum_\Gamma \tilde{V}_{1,ij}^\Gamma \Lambda_{i,\Gamma 0} \Lambda_{j,\Gamma 0}$$
$$+ \frac{1}{2} \sum_{ij} \sum_{\Gamma,a} \tilde{V}_{2,ij}^\Gamma \Lambda_{ij,\Gamma a} \Lambda_{ji,\Gamma a}, \quad (30)$$

where the new interaction parameters $\tilde{V}_{1,ij}^\Gamma$ and $\tilde{V}_{2,ij}^\Gamma$ are given by

$$\tilde{V}_{1,ij}^\Gamma = \sum_{\alpha\beta} Y_{\alpha\alpha}^\Gamma V_{ij}^{\alpha\beta} Y_{\beta\beta}^\Gamma, \quad \tilde{V}_{2,ij}^\Gamma = -\frac{1}{2} \sum_{\alpha\beta} Y_{\alpha\beta}^\Gamma V_{ij}^{\alpha\beta} Y_{\beta\alpha}^\Gamma, \quad (31)$$

and $\Lambda_{i,\Gamma a} \equiv \Lambda_{ii,\Gamma a} = \Lambda_{i,\Gamma a}^\dagger$. The first term is an interaction of pure spin-singlet onsite bilinears, whereas the second term corresponds to the interaction of particle-hole bilinear on bonds or sites.

The same approach applies to the exchange interaction terms $J_{1,2,3}$, as we describe in detail in Appendix E. This leads to a form of H_I given by

$$H_I = \frac{1}{2} \sum_{ij} \sum_{\Gamma,a} \tilde{U}_{1,ij}^{\Gamma a} \Lambda_{i,\Gamma a} \Lambda_{j,\Gamma a}$$
$$+ \frac{1}{2} \sum_{ij} \sum_{\Gamma,a} \tilde{U}_{2,ij}^{\Gamma a} \Lambda_{ij,\Gamma a} \Lambda_{ji,\Gamma a}, \quad (32)$$

with effective particle-hole interactions $\tilde{U}_{1,ij}^{\Gamma a}$ and $\tilde{U}_{2,ij}^{\Gamma a}$.

Before proceeding to a more general analysis of (32), we examine its structure in the limit where only onsite interactions are considered, such that the interactions are parametrized by the coefficients U and J [see Eq. (7)]. As is clear from (32), in this case the interaction parameters can be grouped into $\tilde{U}^{\Gamma a} = \tilde{U}_{1,ii}^{\Gamma a} + \tilde{U}_{2,ii}^{\Gamma a}$, which then define the irreducible bare particle-hole coupling constants. The expressions for $\tilde{U}^{\Gamma a}$ in terms of U and J are given in Table II. The particle-hole channels corresponding to these couplings describe distinct types of particle-hole order, in the same way that different pairing channels describe distinct types of pairing. Spin-singlet channels may also be viewed as charge channels since spin-rotation invariance is preserved. For instance, spin-singlet order with A_2 symmetry corresponds to an ordered state with orbital magnetism, whereas singlet order

TABLE III. Effective interactions for bond particle-hole order involving a pair of sites (ij). Six different channels can be distinguished based on the spin (i.e., singlet or triplet) and orbital structure of the particle-hole channel. Here, we have assumed $V_{ij}^{\alpha\beta} = V_{ij}$, $J_{1,ij}^{\alpha\beta} = J_{1,ij}$, and $J_2 = J_3 = 0$, which corresponds to parameter values considered in Ref. [21].

Neighbors $\tilde{U}_{1,2,ij}^{\Gamma a}$		$\Gamma = A_1$	$\Gamma = A_2$	$\Gamma = E$
$\tilde{U}_{1,ij}^{\Gamma a}$	Singlet	$(4V_{ij} - J_{1,ij})/8$	$-J_{1,ij}/8$	$-J_{1,ij}/8$
	Triplet	$-J_{1,ij}/8$	$-J_{1,ij}/8$	$-J_{1,ij}/8$
$\tilde{U}_{2,ij}^{\Gamma a}$	Singlet	$(4J_{1,ij} - V_{ij})/8$	$-V_{ij}/8$	$-V_{ij}/8$
	Triplet	$-V_{ij}/8$	$-V_{ij}/8$	$-V_{ij}/8$

with E symmetry corresponds to nematic orbital order, which breaks (threefold) rotational symmetry.

In a similar manner, we can explicitly express the effective interactions $\tilde{U}_{1,ij}^{\Gamma a}$ and $\tilde{U}_{2,ij}^{\Gamma a}$ for a bond connecting a pair of distinct sites i and j in terms of V and $J_{1,2,3}$ defined in Eq. (6). For the special case $V_{ij}^{\alpha\beta} = V_{ij}$, $J_{1,ij}^{\alpha\beta} = J_{1,ij}$, and $J_2 = J_3 = 0$ the result is presented in Table III. This particular choice of interaction parameters corresponds to the extended Hubbard model considered in Ref. [21].

We then return to a more general analysis of (32). As in the case of pairing, it is convenient to make use of translational invariance and transform to momentum space. The Fourier transform of the particle-hole operators $\Lambda_{ij,\Gamma a}$ is given by

$$\Lambda_{ij,\Gamma a} = \frac{1}{N} \sum_{\mathbf{q},\mathbf{k}} \Lambda_{\mathbf{k}\nu_i\nu_j,\Gamma a}(\mathbf{q}) e^{i\mathbf{q}\cdot\mathbf{R}_{ij} + i\mathbf{k}\cdot\mathbf{r}_{ij}}, \quad (33)$$

where $\mathbf{r}_{ij} = \mathbf{r}_i - \mathbf{r}_j$ as before, and $\mathbf{R}_{ij} = (\mathbf{r}_i + \mathbf{r}_j)/2$ is the center-of-mass position. As in Eq. (18) the Fourier transform introduces sublattice indices $\nu_i, \nu_j = A, B$. The Fourier transform of the onsite operators $\Lambda_{i,\Gamma a}$ further simplifies and is defined as $\Lambda_{\nu,\Gamma a}(\mathbf{q}) = \sum_{\mathbf{k}} \Lambda_{\mathbf{k}\nu\nu,\Gamma a}(\mathbf{q})$. Substituting (33) into Eq. (32) and performing the sums over site indices, the interaction Hamiltonian takes the form

$$H_I = \frac{1}{2N} \sum_{\mathbf{q}} \sum_{\Gamma,a} \tilde{U}_1^{\Gamma a}(\mathbf{q}) \Lambda_{\Gamma a}^\dagger(\mathbf{q}) \Lambda_{\Gamma a}(\mathbf{q})$$

$$+ \frac{1}{2N} \sum_{\mathbf{q},\mathbf{k}\mathbf{k}'} \sum_{\Gamma,a} \tilde{U}_2^{\Gamma a}(\mathbf{k} - \mathbf{k}') \Lambda_{\mathbf{k}',\Gamma a}^\dagger(\mathbf{q}) \Lambda_{\mathbf{k},\Gamma a}(\mathbf{q}), \quad (34)$$

where we have suppressed sublattice indices ν, ν' to avoid cumbersome expressions. The Fourier transform of the interaction parameters $\tilde{U}_{1,ij}^{\Gamma a}$ is given by (reinstating sublattice indices)

$$\tilde{U}_{1,\nu\nu'}^{\Gamma a}(\mathbf{q}) = \sum_{\mathbf{r}_{ij}} \tilde{U}_{1,ij}^{\Gamma a} e^{-i\mathbf{q}\cdot\mathbf{r}_{ij}}, \quad (35)$$

and similarly for $\tilde{U}_{1,ij}^{\Gamma a}$. As may be seen from (34), the first term is now diagonal. As far as the second term is concerned, we can follow a similar approach as in the pairing case [see Eq. (19)], and write $\tilde{U}_{2,\nu\nu'}^{\Gamma a}(\mathbf{k} - \mathbf{k}')$ as a sum over lattice harmonics. The lattice harmonics are then associated with the particle-hole operators $\Lambda_{\mathbf{k}\nu\nu',\Gamma a}(\mathbf{q})$ and $\Lambda_{\mathbf{k}'\nu\nu',\Gamma a}^\dagger(\mathbf{q})$ to form fully symmetrized particle-hole operators.

The Hamiltonian of Eq. (34) describes the effective interactions of the particle-hole instabilities and provides a natural framework for further analyze them. To determine which instability is strongest within RPA, for instance, the next step is to calculate the particle-hole bubbles in each of the irreducible channels. This is greatly simplified by the fully symmetrized form of the interaction.

We conclude this section by noting that an analysis of the particle-hole instabilities in "higher angular momentum" channels, that is to say, instabilities in channels corresponding to lattice harmonics and governed by $\tilde{U}_2^{\Gamma a}(\mathbf{k} - \mathbf{k}')$, is particularly relevant in TBG. As pointed out in Ref. [31], a natural candidate for the ordered insulating state at quarter-filling is a magnetic state for which the magnetic moments reside on the honeycomb bonds. As a result, this is a bond-spin ordered state which occurs in a particle-hole channel corresponding to nontrivial lattice harmonics.

V. SPIN-ORBITAL EXCHANGE MODEL AT QUARTER-FILLING

The analysis of the previous sections focused entirely on the interacting part of the Hamiltonian H_I, classifying the irreducible particle-particle and particle-hole channels. To obtain a phase diagram, it is necessary to include also the kinetic term H_K. This can be done in a controlled way in two different regimes: weak coupling, where H_I is treated perturbatively, or strong coupling, where H_K is treated perturbatively. The small bandwidth ($W \sim 10$ meV) of the nearly flat bands in TBG does not immediately suggest the weak-coupling approach as a natural starting point to address electronic correlations in TBG. Indeed, estimates for the onsite Coulomb repulsion U indicate that $U \gtrsim W$ [1], placing the system in a moderately correlated regime. To assess this regime, in this section we opt to start from the strong-coupling limit in which the onsite interaction U is much larger than the bandwidth.

In this case, the extended Hubbard model discussed in Sec. II can be studied by considering the interactions first and then treating the kinetic part as a perturbation in $\sim t/U$. This amounts to integrating out the charge degree of freedom and results in an effective model for the spin and orbital variables. Spin-orbital exchange models of this Kugel-Khomskii type [70,71] have proven rather successful in describing a large class of strongly correlated multiorbital systems [72–75]. The key difference between the latter and TBG is the microscopic nature of the orbital degree of freedom, which does not correspond to an atomic orbital in TBG. Instead, the localized Wannier states of the flat bands are associated with the Moiré superlattice. As a result, the aim of this section is to explore to what extent standard approaches from correlated multiorbital systems can be applied to TBG.

A. Derivation of the effective Hamiltonian

To proceed, we consider the interacting Hamiltonian given by (7), which only includes the onsite interactions. Restricting the interaction to onsite terms only is an oversimplification for TBG, but necessary for the purpose of deriving a spin-orbital model. The onsite Coulomb repulsion of (7) reorganizes the Hilbert space based on the number of electrons per site,

assigning an energy cost to multiple occupancy. Since the insulating behavior of TBG was observed for one electron per site (or two electrons per Moiré supercell), we focus on this case and define the low-energy subspace by all configurations for which each site is singly occupied.

To obtain the effective Hamiltonian $\mathcal{H}$ we follow the standard approach and consider virtual superexchange processes via excited states with two electrons per site. This amounts to diagonalizing the interacting Hamiltonian H_I and treating the kinetic Hamiltonian H_K as a perturbation. In Sec. III we diagonalized (7) in the two-particle sector and obtained the energies of the intermediate excited states given in Table I. The effective Hamiltonian can then be viewed as an expansion in $\sim t/U$. Considering all hopping processes into the higher-energy sector and back, $\mathcal{H}$ can be expressed in the general form

$$\mathcal{H} = \mathcal{P} H_K^\dagger \frac{1}{\varepsilon_0 - H_I} H_K \mathcal{P}, \tag{36}$$

where $\mathcal{P}$ are projectors onto the low-energy subspace. As is usual, the effective Hamiltonian is governed by the superexchange energy scale $\sim t^2/U$. Since the virtual superexchange processes occur on one particular bond (ij), it suffices to derive the Hamiltonian $\mathcal{H}_{ij}$ for one such bond; the full Hamiltonian $\mathcal{H}$ is given by a sum over all bonds. In principle, a superexchange coupling of spin and orbital variables can be obtained for any pair of sites (ij) connected by H_K. In what follows, we focus attention on the simplest case, which only includes nearest-neighbor hopping. Further-neighbor terms can be derived and analyzed analogously. In this situation, the hopping along each bond can be parametrized by $t_\sigma = t_1 + t_1'$ and $t_\pi = t_1 - t_1'$ in an appropriate basis [see Eq. (3) and Appendices A and B].

Since the microscopic Hamiltonian $H = H_K + H_I$ is SU(2) spin rotationally invariant, the effective low-energy Hamiltonian must also be SU(2) invariant, which implies that the effective Hamiltonian $\mathcal{H}_{ij}$ for a bond (ij) is constructed from the projectors $\mathcal{P}_{ij}^{S=0}$ and $\mathcal{P}_{ij}^{S=1}$ onto total spin states $S = 0$ and 1 of the electrons connected by the bond. The projectors onto the singlet and triplet states are given by

$$\mathcal{P}_{ij}^{S=0} = \tfrac{1}{4} - \mathbf{S}_i \cdot \mathbf{S}_j, \quad \mathcal{P}_{ij}^{S=1} = \tfrac{3}{4} + \mathbf{S}_i \cdot \mathbf{S}_j, \tag{37}$$

where $\mathbf{S}_i$ describes the spin of site i.

In addition to the spin variables, the superexchange Hamiltonian acts on the orbital variables. This action can be described by the orbital Pauli matrices $\boldsymbol{\tau}_i = (\tau_i^z, \tau_i^x, \tau_i^y)$, where $\tau_i^z = \pm 1$ corresponds to occupancy of the p_x, p_y orbital on site i. Note the particular ordering of the Pauli matrices in the definition of $\boldsymbol{\tau}_i$. To capture the action of the superexchange Hamiltonian on the orbital variables, it convenient to introduce orbital projection operators, by analogy with (37). We introduce the projection operators $\mathcal{P}_{ij}^{\alpha\beta}$ given by

$$\mathcal{P}_{ij}^{xx} = (1 + \hat{\mathbf{e}}_{ij} \cdot \boldsymbol{\tau}_i)(1 + \hat{\mathbf{e}}_{ij} \cdot \boldsymbol{\tau}_j)/4, \tag{38}$$

$$\mathcal{P}_{ij}^{xy} = (1 + \hat{\mathbf{e}}_{ij} \cdot \boldsymbol{\tau}_i)(1 - \hat{\mathbf{e}}_{ij} \cdot \boldsymbol{\tau}_j)/4, \tag{39}$$

where $\hat{\mathbf{e}}_{ij}$ is a unit vector in the direction of the bond (ij). Therefore, $\hat{\mathbf{e}}_{ij}$ can take the values $\hat{\mathbf{e}}_{n=1,2,3}$, which are shown in Fig. 4. The projection operator $\mathcal{P}_{ij}^{xx}$, for instance, projects

on states for which the $p_x' = (p_x \hat{\mathbf{e}}_x + p_y \hat{\mathbf{e}}_y) \cdot \hat{\mathbf{e}}_{ij}$ orbital is occupied on both sites i and j. Note that this is the p_x orbital in a basis defined by the bond directions $(\hat{\mathbf{e}}_{ij}, \hat{\mathbf{e}}_{ij}^\perp)$ rather than $(\hat{\mathbf{e}}_x, \hat{\mathbf{e}}_y)$ [79] (see Appendix F for details). In the case $\hat{\mathbf{e}}_{ij} = \hat{\mathbf{e}}_1 = (1, 0)^T$ the projector $\mathcal{P}_{ij}^{xx}$ takes the form $(1 + \tau_i^z)(1 + \tau_j^z)/4$. The projector $\mathcal{P}_{ij}^{xy}$ projects on states for which the $p_x' = (p_x \hat{\mathbf{e}}_x + p_y \hat{\mathbf{e}}_y) \cdot \hat{\mathbf{e}}_{ij}$ orbital is occupied on site i and the $p_y' = (p_x \hat{\mathbf{e}}_x + p_y \hat{\mathbf{e}}_y) \cdot \hat{\mathbf{e}}_{ij}^\perp$ orbital is occupied on site j (both in a bond-dependent basis). The projection operators $\mathcal{P}_{ij}^{yy}$ and $\mathcal{P}_{ij}^{yx}$ are obtained from (38) and (39) by inverting the signs.

To describe all superexchange processes, one must also account for the possibility that orbital flavors are flipped or exchanged. For this purpose we introduce operators that flip the orbital occupation of the sites i and j; these operators are given by

$$\mathcal{Q}_{ij} = (\tau_i^+ \tau_j^+ + \tau_i^- \tau_j^-)/2, \tag{40}$$

$$\bar{\mathcal{Q}}_{ij} = (\tau_i^+ \tau_j^- + \tau_i^- \tau_j^+)/2, \tag{41}$$

where $\tau_i^\pm$ and $\tau_i^\pm$ flip the orbital occupation on site i and j in a basis defined by the bond directions $(\hat{\mathbf{e}}_{ij}, \hat{\mathbf{e}}_{ij}^\perp)$, as before. For a bond along $\hat{\mathbf{e}}_{ij} = \hat{\mathbf{e}}_1$ the operator $\tau_i^\pm$ takes the form $\tau_i^\pm = \tau_i^x \pm i \tau_i^y$ (see Appendix F). Clearly, the $\mathcal{Q}_{ij}$ matrix elements are nonzero only in the subspace of equal occupation, whereas $\bar{\mathcal{Q}}_{ij}$ only acts within the subspace of opposite orbital occupation.

Making use of these operators and carefully examining all superexchange processes to obtain the correct coefficients, we find that the nearest-neighbor spin-orbital superexchange Hamiltonian $\mathcal{H}$ is given by

$$\begin{aligned}
\mathcal{H} = \sum_{\langle ij \rangle} \Bigg\{ &\frac{1}{U - 3J} \mathcal{P}_{ij}^{S=1} \big[t_\sigma t_\pi \bar{\mathcal{Q}}_{ij} - (t_\sigma^2 + t_\pi^2)(\mathcal{P}_{ij}^{xy} + \mathcal{P}_{ij}^{yx}) \big] \\
&- \frac{1}{U + J} \mathcal{P}_{ij}^{S=0} \big(t_\sigma t_\pi \mathcal{Q}_{ij} + 2 t_\sigma^2 \mathcal{P}_{ij}^{xx} + 2 t_\pi^2 \mathcal{P}_{ij}^{yy} \big) \\
&+ \frac{1}{U - J} \mathcal{P}_{ij}^{S=0} \big[t_\sigma t_\pi (\mathcal{Q}_{ij} - \bar{\mathcal{Q}}_{ij}) - 2 t_\sigma^2 \mathcal{P}_{ij}^{xx} - 2 t_\pi^2 \mathcal{P}_{ij}^{yy} \\
&- (t_\sigma^2 + t_\pi^2)(\mathcal{P}_{ij}^{xy} + \mathcal{P}_{ij}^{yx}) \big] \Bigg\}.
\end{aligned} \tag{42}$$

Here, the sum is over honeycomb nearest-neighbor sites $\langle ij \rangle$. In its most general form given by (42) the Hamiltonian describes a rather complicated coupling between spin and orbital variables, parametrized by the two hopping integrals $t_{\sigma,\pi}$ and the interaction terms U, J. This Hamiltonian can be compared to similar spin-orbital Hamiltonians obtained in the context of correlated multiorbital models for transition-metal oxides [91,92].

In the present case, while (42) includes nearest-neighbor couplings only, the superexchange Hamiltonian can be systematically extended to include further-neighbor spin-orbital superexchange couplings. This will generate superexchange terms of a similar type as in Eq. (42), but for bonds (ij) corresponding to second- and further-nearest-neighbor sites. Using the machinery developed in our work, it is in principle straightforward to obtain these additional terms by including hopping processes such as Eqs. (4) and (5) in H_K of (36), but

is expected to introduce frustration. A detailed study of the resulting phase diagram is beyond the scope of this work.

A natural first step to study (42) is to consider a mean-field theory and replace the spin and orbital operators by classical variables. This is the approach we take there.

B. Mean-field solution in the isotropic limit

While a full phase diagram for arbitrary values of t_σ and t_π can in principle be obtained by, for instance, Monte Carlo simulations, this is beyond the scope of our work. Rather, we develop a mean-field theory based on an assumption which directly derives from the reported properties of TBG. Both first-principles as well as tight-binding calculations show that the low-energy bands of TBG are well described by the approximation $t_\sigma \approx t_\pi$ [21]. Therefore, here we focus on the isotropic case $t_\sigma = t_\pi \equiv t$, for which the spin-orbital Hamiltonian (42) simplifies and reads as

$$
\mathcal{H} = \sum_{\langle ij \rangle} \left\{ \frac{t^2}{(U-3J)} \left(\frac{3}{4} + \mathbf{S}_i \cdot \mathbf{S}_j \right) (\boldsymbol{\tau}_i \cdot \boldsymbol{\tau}_j - 1) \right.
$$
$$
- \frac{t^2}{U+J} \left(\frac{1}{4} - \mathbf{S}_i \cdot \mathbf{S}_j \right) \left(1 + \boldsymbol{\tau}_i \cdot \boldsymbol{\tau}_j - 2\tau_i^y \tau_j^y \right)
$$
$$
\left. - \frac{2t^2}{U-J} \left(\frac{1}{4} - \mathbf{S}_i \cdot \mathbf{S}_j \right) \left(\tau_i^y \tau_j^y + 1 \right) \right\}. \quad (43)
$$

This Hamiltonian clearly reflects the higher U(1) orbital symmetry that results from the neglecting the hopping anisotropy. In this form, the Hamiltonian bears resemblance to an SU(4) symmetric spin-orbital model on the hyperhoneycomb lattice [93].

Before proceeding, let us briefly review the meaning of the different degrees of freedom appearing in this Hamiltonian. A finite expectation value $\langle \mathbf{S}_i \rangle$ simply implies long-range magnetic order since $\mathbf{S}_i$ is simply the spin at site i, whose magnitude is here set to $\frac{1}{2}$. A finite expectation value $\langle \boldsymbol{\tau}_i \rangle$ implies some form of orbital order, which depends on the direction of $\boldsymbol{\tau}_i$ (its magnitude here is set to 1). A finite $\langle \tau_i^z \rangle$ implies that the occupation of the p_x and p_y orbitals are not the same in site i. This breaks rotational symmetry and is therefore an orbital-nematic order. The same is true for $\langle \tau_i^x \rangle$, but with the difference that $p_x + p_y$ and $p_x - p_y$ orbitals are split in energy. Therefore, it is convenient to construct the two-dimensional vector $\langle \boldsymbol{\tau}_i^\parallel \rangle = \langle \tau_i^x \rangle \hat{\mathbf{x}} + \langle \tau_i^z \rangle \hat{\mathbf{z}}$, which behaves as an XY nematic order parameter. In contrast to $\langle \boldsymbol{\tau}_i^\parallel \rangle$, a finite $\langle \tau_i^y \rangle$ does not break rotational symmetry but instead breaks time-reversal symmetry by selecting one of the two orbital angular momentum eigenstates $p_x \pm ip_y$. Consequently, a finite $\langle \tau_i^y \rangle$ implies long-range orbital-magnetic order.

Because the honeycomb superlattice is bipartite, we can find the mean-field classical ground state by computing the classical energy of a single bond E_{bond}. Since the Hamiltonian (43) is SU(2) invariant in spin-space, there are only two possible classical spin ground states, ferromagnetic (FM) or antiferromagnetic (AFM). We can thus find the orbital ground states in these two cases and compare their energies to find the minimum.

Let us start with the AFM case. Defining $\Delta = t^2/U$, the bond energy is given by

$$
\frac{E_{\text{bond}}^{(\text{AFM})}}{\Delta} = E_0^{(\text{AFM})} + K_\parallel \boldsymbol{\tau}_i^\parallel \cdot \boldsymbol{\tau}_j^\parallel + K_y \tau_i^y \tau_j^y, \quad (44)
$$

where we defined

$$
E_0^{(\text{AFM})} = \frac{2U(J^2 + 2JU - U^2)}{(U^2 - J^2)(U - 3J)},
$$
$$
K_\parallel = \frac{2JU(U - J)}{(U^2 - J^2)(U - 3J)},
$$
$$
K_y = \frac{4J^2 U}{(U^2 - J^2)(U - 3J)}. \quad (45)
$$

Before we proceed, we first need to discuss the range of J/U values that is reasonable. Since $U' = U - 2J$, in order to have $U' > 0$, we must have $J/U < \frac{1}{2}$. Here, we allow J to be negative as well, which would imply violation of Hund's first rule. This was also proposed in the context of TBG in Ref. [12]. Consequently, in what follows, we consider the range $-\frac{1}{2} < J/U < \frac{1}{2}$.

The orbital ground state can be obtained by analyzing the orbital exchange constants $K_\parallel$ and K_y as function of J. It follows that $|K_\parallel| \geqslant |K_y|$ for $-\frac{1}{2} < J/U < \frac{1}{3}$. Thus, in this range, the energy is minimized by an orbital-nematic configuration. Since $K_\parallel < 0$ for $J < 0$, this gives ferro-orbital (FO) nematic order. On the other hand, because $K_\parallel > 0$ for $J > 0$, we obtain antiferro-orbital (AFO) nematic order. Similarly, because $|K_\parallel| < |K_y|$ for $\frac{1}{3} < J/U < \frac{1}{2}$, the configuration that minimizes the bond energy is orbital-magnetic order. As $K_y < 0$ in this range, we obtain a ferro-orbital magnetic order.

Now, let us consider the FM case. The bond energy is

$$
\frac{E_{\text{bond}}^{(\text{FM})}}{\Delta} = E_0^{(\text{FM})} + K \boldsymbol{\tau}_i \cdot \boldsymbol{\tau}_j \quad (46)
$$

with

$$
E_0^{(\text{FM})} = -\frac{U}{U - 3J}, \quad K = \frac{U}{U - 3J}. \quad (47)
$$

Note that the FM bond energy is invariant under SU(2) rotations in orbital space. This "accidental" symmetry stems from the approximations we employed to derive the effective Hamiltonian, and will likely be removed if further-neighbor hoppings are included. In any case, there is a degeneracy in this situation between orbital-nematic and orbital-magnetic orders. For this reason, hereafter we will refer to this configuration as SU(2) orbital order.

Minimization of the bond energy (46) is straightforward: for $J/U < \frac{1}{3}$, the orbital-exchange coefficient $K > 0$ and we obtain antiferro SU(2) orbital order. On the other hand, for $J/U > \frac{1}{3}$, we find SU(2) ferro-orbital order since $K < 0$.

Having minimized the bond energies of the AFM and FM spin configurations, we compare them to find the global bond-energy minimum. The result is shown in Fig. 5, and comprises three regimes: for $-\frac{1}{2} < J/U < 0$, the configuration that minimizes E_{bond} is an antiferromagnetic (AFM) and ferro-orbital (FO) nematic order. For $0 < J/U < \frac{1}{3}$, the bond energy is minimized by a ferromagnetic (FM) and antiferro-orbital (AFO) SU(2) order. Finally, for $\frac{1}{3} < J/U < \frac{1}{2}$, the system's configuration corresponds to AFM and ferro-orbital
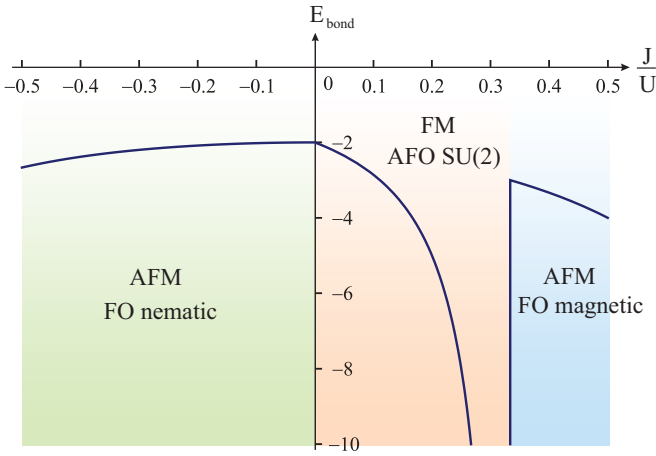
FIG. 5. Phase diagram of the classical mean-field solution of the spin-orbital exchange model in the isotropic case ($t_\sigma = t_\pi$), obtained by minimizing the bond energy E_{bond} (here plotted in units of $\Delta = t^2/U$) as function of the ratio J/U. AFM refers to antiferromagnetic order, FM to ferromagnetic order, FO to ferro-orbital order, and AFO to antiferro-orbital order. For $J < 0$, the orbital order lowers the point-group symmetry of the honeycomb lattice, and is thus nematic [Fig. 1(a)]. For $0 < J < U/3$, there is an enlarged SU(2) symmetry in the orbital degrees of freedom, and the orbital order can be either nematic or magnetic [Fig. 1(b) illustrates the nematic case]. For $J > U/3$, the system has orbital-magnetic order [Fig. 1(c)].

(FO) magnetic order. Note that in all cases translational symmetry is broken.

We note that our strong-coupling expansion is formally not valid in the vicinity of $J/U = \frac{1}{3}$, since in this case one of the denominators of the effective Hamiltonian (42) diverges. Note also that, for $J = 0$, the system has additional symmetries, signaled here by the fact that different configurations minimize the bond energy.

VI. CONCLUDING REMARKS

In this paper, we analyzed the possible electronic orders arising from the two-orbital extended Hubbard model on the honeycomb lattice, which has been proposed to describe the nearly flat bands of TBG. First, we presented a general framework to decompose the several interaction terms into different irreducible particle-particle and particle-hole channels. Although such a framework is suitable for both weak-coupling and strong-coupling calculations, here we focused on the latter. As a result, we derived a spin-orbital exchange model for the quarter-filling Mott insulating state. Its mean-field solution in the isotropic limit unveils a rich intertwinement between orbital and spin degrees of freedom, analogous to the physics of certain correlated multiorbital transition-metal oxides. We also discussed the possibility of vestigial superconducting phases, which are likely to be realized in TBG if the ground state is d wave or p wave, given the two-dimensional character of TBG. While further experiments are needed to shed light on the types of electronic order realized in TBG, the general framework established here provides a solid starting point to assess the impact of correlations on the spin, charge, and orbital degrees of freedom of this system.

APPENDIX A: ROTATIONS IN WANNIER ORBITAL SPACE

The Wannier orbital states of the TBG honeycomb superlattice model proposed in Refs. [5,18,21] have p-wave symmetry and transform as partners of the E representation of D_3. The operators $c_{x,y}^\dagger$ create electrons in the $p_{x,y}$ Wannier states, which are defined with respect to the x and y axes, i.e., a basis defined by $\hat{\mathbf{e}}_x, \hat{\mathbf{e}}_y$. We are free to choose a different basis corresponding to the rotated vectors $\hat{\mathbf{e}}_\varphi, \hat{\mathbf{e}}_\varphi^\perp$ defined in (2). The rotated orbitals $p'_{x,y}$ can be expressed as $p'_x = (p_x \hat{\mathbf{e}}_x + p_y \hat{\mathbf{e}}_y) \cdot \hat{\mathbf{e}}_\varphi$ and $p'_y = (p_x \hat{\mathbf{e}}_x + p_y \hat{\mathbf{e}}_y) \cdot \hat{\mathbf{e}}_\varphi^\perp$. This defines a rotation matrix $U_\varphi \equiv e^{-i\varphi\tau^y}$, corresponding to a rotation by an angle φ about the z axis:

$$\begin{pmatrix} p'_x \\ p'_y \end{pmatrix} = U_\varphi^\dagger \begin{pmatrix} p_x \\ p_y \end{pmatrix}. \tag{A1}$$

The operators creating (annihilating) electrons in the rotated orbitals $p'_{x,y}$ are then given by $c^\dagger U_\varphi$ ($U_\varphi^\dagger c$). The matrix U_φ is a representation of rotations $C_{\varphi z}$ about the z axis generated by τ^y. Recall that U_φ is not a symmetry for general φ, but only for $\varphi_n = 2\pi n/3$ in the case of the D_3 point group.

The rotations of the orbitals given in Eq. (A1) imply a rotation of the Pauli matrices $\boldsymbol{\tau}$. Consider first the pair of Pauli matrices (τ^z, τ^x). Under rotations in orbital space the Pauli matrices transform as

$$U_\varphi \tau^z U_\varphi^\dagger = \cos 2\varphi \, \tau^z + \sin 2\varphi \, \tau^x, \tag{A2}$$

$$U_\varphi \tau^x U_\varphi^\dagger = -\sin 2\varphi \, \tau^z + \cos 2\varphi \, \tau^x. \tag{A3}$$

This shows that the two Pauli matrices transform as partners under rotations and that they have d-wave symmetry:

$$C_{\varphi z} : \begin{pmatrix} \tau^z \\ \tau^x \end{pmatrix} \rightarrow U_{2\varphi}^\dagger \begin{pmatrix} \tau^z \\ \tau^x \end{pmatrix}. \tag{A4}$$

We can also define the matrices $U_x = \tau_z$ and $U_y = -\tau_z$ that represent the twofold rotations about the x axis (C_{2x}) and y axis (C_{2y}), respectively. Under either of these transformations, (τ^z, τ^x) → ($\tau^z, -\tau^x$). Meanwhile, the Pauli matrix τ^y is invariant under $C_{\varphi z}$ rotations but odd under C_{2y} and C_{2x} rotations. This implies that (τ^z, τ^x) have E symmetry under D_3 and τ^y has A_2 symmetry.

The form of the rotation matrix $U_\varphi \equiv e^{-i\varphi\tau^y}$ implies that it is diagonal in a basis in which τ^y is diagonal. This basis is defined by the orbitals complex orbitals $p_\pm = p_x \pm i p_y$, which are eigenvectors of the angular momentum projections $L_z = \pm 1$. If we define $c_\pm$ as the operators corresponding to $p_\pm$, then one has $C_{\varphi z} : c_\pm \rightarrow e^{\pm i\varphi} c_\pm$. This implies that if the terms in the kinetic Hamiltonian (1) do not couple c_+ and c_-, which is only true for a specific set of (fine-tuned) hopping parameters, the kinetic Hamiltonian H_K has a larger U(1) symmetry given by $C_{\varphi z}$. Since the orbitals $p_\pm$ can be related

to the valley degrees of freedom of the constituent graphene layers [21], this larger symmetry can be associated with a U(1) valley symmetry.

APPENDIX B: HOPPING MATRIX SYMMETRY CONSTRAINTS FOR D_3 MODEL

In this appendix, we review the symmetry constraints on the hopping matrices discussed in Ref. [18] using a different formalism.

The kinetic Hamiltonian of Eq. (1) defines the hopping matrices $\hat{T}(\mathbf{r}_{ij})$, where $\mathbf{r}_{ij}$ is the distance between sites forming the bond (ij). It is natural to group the set of hopping matrices into subsets defined by fixed distance $\mathbf{r}_{ij}$, which is a grouping based on nearest neighbors, and we introduce the index γ to denote the γth nearest-neighbor bonds. That is, $\gamma = 1, 2, 3$ denotes the first-, second-, and third-nearest neighbors. We then rewrite the set of hopping matrices as $\hat{T}_n^{(\gamma)}$, where $n = 1, \ldots, N_\gamma$ is an index for all the γth nearest neighbors, of which there are N_γ.

For given γ one may then obtain symmetry constraints for $\hat{T}_n^{(\gamma)}$, from which the number of independent hopping parameters can be determined. As an example, consider the first-nearest neighbor ($\gamma = 1$) hopping matrix for $n = 1$. Due to time-reversal symmetry there exists a gauge in which all matrix elements of $\hat{T}_1^{(1)}$ are real and the hopping matrix can be expanded in orbital Pauli matrices as

$$\hat{T}_1^{(1)} = t_{10} + t_{1z}\tau^z + t_{1x}\tau^x + it_{1y}\tau^y, \tag{B1}$$

where $(t_{10}, t_{1x}, t_{1y}, t_{1z})$ are four real parameters. The twofold rotation C_{2y} gives rise to constraints on these parameters. Abbreviating $\hat{T}_{n=1}^{(1)}$ as $\hat{T}$ for simplicity, the constraints can be stated as

$$C_{2y} \; \rightarrow \; \tau^z \hat{T} \tau^z = \hat{T}^\dagger. \tag{B2}$$

The appearance of $\hat{T}^\dagger$ on the right-hand side of the constraint (B2) is due to the fact that C_{2y} exchanges the sites connected by the bond. The constraint (B2) forces $t_{1x} = 0$, which would lead to three independent hopping parameters. As noted in Ref. [18], however, with a redefinition of the basis of the two Wannier states one of these can be absorbed. It is natural to choose t_{1y} and this leads to Eq. (3) with $(t_{10}, t_{1z}) \equiv (t_1, t_1')$. Since we have now fixed the basis of the Wannier states, no further symmetry-allowed hopping parameters (of further-neighbor bonds) can be absorbed by redefinition.

The two remaining first-nearest-neighbor hopping matrices $T_{2,3}^{(1)}$ follow directly from $T_1^{(1)}$ by performing threefold rotations:

$$\hat{T}_2^{(1)} = U_{\varphi_2} \hat{T}_1^{(1)} U_{\varphi_2}^\dagger, \quad \hat{T}_3^{(1)} = U_{\varphi_3} \hat{T}_1^{(1)} U_{\varphi_3}^\dagger, \tag{B3}$$

where $\varphi_n = 2\pi(n-1)/3$ are the angles of the nearest-neighbor unit vectors (see Sec. II).

The same analysis can be applied to any of the other inter-sublattice hopping matrices, i.e., those matrices corresponding to bonds connecting sites on different sublattices. We take the third-nearest-neighbor hopping (i.e., across a hexagon) as an example and expand

$$\hat{T}_1^{(3)} = t_{30} + t_{3z}\tau^z + t_{3x}\tau^x + it_{3y}\tau^y, \tag{B4}$$

where $(t_{30}, t_{3x}, t_{3y}, t_{3z})$ are again four real parameters. Now, abbreviating $\hat{T}_{n=1}^{(3)}$ as $\hat{T}$ we find the constraint from C_{2y} as

$$C_{2y} \; \rightarrow \; \tau^z \hat{T} \tau^z = \hat{T}^\dagger. \tag{B5}$$

This is the same constraint as (B2) and we conclude that $t_{3x} = 0$. As a result, $\hat{T}_1^{(3)}$ has three real parameters and is given by $\hat{T}_1^{(3)} = t_3 + t_3'\tau^z + it_3''\tau^y$. The remaining third-nearest-neighbor hopping matrices are found by rotation as in Eq. (B3).

Next, consider intrasublattice hoppings associated with bonds connecting sites on the same sublattice. The simplest example is second-nearest-neighbor ($\gamma = 2$) hopping. (This is first-nearest-neighbor hopping on the triangular sublattice.) Again, we start from $n = 1$, i.e., $\hat{T}_1^{(2)}$, which corresponds to the second-nearest-neighbor bond along the direction of $\mathbf{a}_1$ in Fig. 4. As before, we expand

$$\hat{T}_1^{(2)} = t_{20} + t_{2z}\tau^z + t_{2x}\tau^x + it_{2y}\tau^y, \tag{B6}$$

with real coefficients. To determine the symmetry constraints on the coefficients, we must account for the two sublattices A and B. We abbreviate $\hat{T}_1^{(2)}$ on the A (B) sublattice as $\hat{T}_A$ ($\hat{T}_B$) and find that the constraints from the twofold rotation C_{2y} are given by

$$C_{2y} \; \rightarrow \; \tau^z \hat{T}_A \tau^z = \hat{T}_B. \tag{B7}$$

This equation does not give rise to constraints on the hopping parameters on one sublattice, but instead relates the hopping parameters on the two sublattices. In particular, (t_{20}, t_{2z}) are identical on the two sublattices, whereas (t_{2x}, t_{2y}) have opposite sign.

As a second example of intrasublattice hopping, consider fifth-nearest-neighbor hopping. Fifth-nearest-neighbor hopping, which is second-nearest neighbor on the triangular sublattices, has played an important role in previous work [5,21]. In particular, it was identified as being responsible for the splitting of bands along $\Gamma - M$ in models with an additional U(1) symmetry. Consider the bond defined by the lattice vector $\mathbf{a}_3 - \mathbf{a}_2$; we define the corresponding hopping matrix $\hat{T}_1^{(5)}$ and expand it as before as

$$\hat{T}_1^{(5)} = t_{50} + t_{5z}\tau^z + t_{5x}\tau^x + it_{5y}\tau^y. \tag{B8}$$

For simplicity, we once more abbreviate $\hat{T}_1^{(5)}$ on the A (B) sublattice as $\hat{T}_A$ ($\hat{T}_B$). The constraints from the twofold rotation C_{2y} now read as

$$C_{2y} \; \rightarrow \; \tau^z \hat{T}_A \tau^z = \hat{T}_B^\dagger. \tag{B9}$$

Comparison with Eq. (B7) shows that (B9) leads to a different relation between t_{5y} on the two sublattices. Specifically, one finds that (t_{50}, t_{5z}, t_{5y}) are identical on the two sublattices, whereas only t_{5x} has opposite sign. It is precisely this property of t_{5y} which is responsible for the splitting of bands along $\Gamma - M$.

APPENDIX C: DECOMPOSITION INTO IRREDUCIBLE PAIRING CHANNELS

The pair creation operator $\Pi_{i\alpha\sigma, j\beta\sigma'}^\dagger$ is defined as

$$\Pi_{i\alpha\sigma, j\beta\sigma'}^\dagger = c_{i\alpha\sigma}^\dagger c_{j\beta\sigma'}^\dagger, \tag{C1}$$

such that a two-particle state $|i\alpha\sigma; j\beta\sigma'\rangle$ is given by $|i\alpha\sigma; j\beta\sigma'\rangle = \Pi^{\dagger}_{i\alpha\sigma, j\beta\sigma'}|0\rangle$. Note that this definition implies $\Pi_{i\alpha\sigma, j\beta\sigma'} = c_{j\beta\sigma'}c_{i\alpha\sigma}$. A general pairing operator can be decomposed into irreducible pairing operators with symmetry quantum numbers (Γ, S, M) as

$$\Pi^{\dagger}_{i\alpha\sigma, j\beta\sigma'} = \sum_{\Gamma} \sum_{S,M} X^{\Gamma}_{\alpha\beta} C^{SM}_{\sigma\sigma'} \Pi^{\dagger}_{ij,\Gamma,SM}, \qquad \text{(C2)}$$

where $C^{SM}_{\sigma\sigma'} = C^{SM}_{\frac{1}{2}\sigma\frac{1}{2}\sigma'} = \langle\frac{1}{2}\frac{1}{2}; SM|\frac{1}{2}\sigma; \frac{1}{2}\sigma'\rangle$ are Clebsch-Gordan coefficients. Here, $S = 0$ corresponds to spin-singlet pairing and $S = 1$ corresponds to spin-triplet pairing, in which case M takes values $M = -1, 0, 1$.

Similar to singlet and triplet pairing operators, the operators $\Pi^{\dagger}_{ij,\Gamma}$ (suppressing spin for simplicity) are symmetrized in orbital space and are thus labeled by point-group representations $\Gamma \in \{A_1, A_2, E\}$. Note that E is a two-dimensional d-wave channel. The irreducible pairing operators $\Pi^{\dagger}_{ij,\Gamma}$ are given by

$$\Pi^{\dagger}_{ij,A_1} = \sum_{\alpha\beta} \frac{\delta_{\alpha\beta}}{\sqrt{2}} c^{\dagger}_{i\alpha} c^{\dagger}_{j\beta}, \quad \Pi^{\dagger}_{ij,A_2} = \sum_{\alpha\beta} \frac{\epsilon_{\alpha\beta}}{\sqrt{2}} c^{\dagger}_{i\alpha} c^{\dagger}_{j\beta}, \quad \text{(C3)}$$

$$\left(\Pi^{\dagger}_{ij,E_1}, \Pi^{\dagger}_{ij,E_2}\right) = \frac{1}{\sqrt{2}} \sum_{\alpha\beta} \left(\tau^z_{\alpha\beta}, \tau^x_{\alpha\beta}\right) c^{\dagger}_{i\alpha} c^{\dagger}_{j\beta}. \qquad \text{(C4)}$$

The coefficients $X^{\Gamma}_{\alpha\beta}$ in Eq. (C2) are the analogs of Clebsch-Gordan coefficients for the orbital sector; they are given by

$$X^{A_1}_{\alpha\beta} = \frac{1}{\sqrt{2}} \delta_{\alpha\beta}, \quad X^{A_2}_{\alpha\beta} = \frac{1}{\sqrt{2}} \epsilon_{\alpha\beta}, \qquad \text{(C5)}$$

$$\left(X^{E_1}_{\alpha\beta}, X^{E_2}_{\alpha\beta}\right) = \frac{1}{\sqrt{2}} \left(\tau^z_{\alpha\beta}, \tau^x_{\alpha\beta}\right). \qquad \text{(C6)}$$

Fermi statistics imposes constraints on the decomposition of Eq. (C2), in particular on the set of quantum numbers (Γ, S, M). Spin-singlet and spin-triplet states are antisymmetric and symmetric with respect to particle exchange, respectively; similarly, states with A_2 symmetry are antisymmetric and states with A_1 or E symmetry are symmetric. As a result, when $i = j$ spin-singlet states can only have A_1 or E symmetry, whereas spin-triplet states must have A_2 symmetry. In general, one has the relation

$$\Pi^{\dagger}_{ij,\Gamma,SM} = (-1)^{p_{\Gamma}+p_S+1} \Pi^{\dagger}_{ji,\Gamma,SM}, \qquad \text{(C7)}$$

where p_S is the parity of the spin state (i.e., $p_0 = 1$ and $p_1 = 0$) and p_{Γ} is the parity of the orbital state (i.e., $p_{A_2} = 1$ and zero otherwise).

Substituting Eq. (C2) into H_I of Eq. (6) we arrive at the form

$$H_I = \sum_{ij} \sum_{SM} \sum_{\Gamma} U^{\Gamma}_{ij} \Pi^{\dagger}_{ij,\Gamma,SM} \Pi_{ij,\Gamma',SM}, \qquad \text{(C8)}$$

where matrix elements U^{Γ}_{ij} are defined as

$$U^{\Gamma}_{ij} = V^{\Gamma}_{ij} + J^{\Gamma}_{1,ij} + J^{\Gamma}_{2,ij} + J^{\Gamma}_{3,ij}. \qquad \text{(C9)}$$

The matrix elements V^{Γ}_{ij} are given by Eq. (11); the expressions for the remaining matrix elements are

$$J^{\Gamma}_{1,ij} = (-1)^{p_{\Gamma}+p_S+1} \sum_{\alpha\beta} X^{\Gamma}_{\alpha\beta} (J_1)^{\alpha\beta}_{ij} X^{\Gamma}_{\alpha\beta}, \qquad \text{(C10)}$$

$$J^{\Gamma}_{2,ij} = (-1)^{p_{\Gamma}+p_S+1} \sum_{\alpha\beta} X^{\Gamma}_{\alpha\beta} (J_2)^{\alpha\beta}_{ij} X^{\Gamma}_{\beta\alpha}, \qquad \text{(C11)}$$

$$J^{\Gamma}_{3,ij} = (-1)^{p_{\Gamma}+p_S+1} \sum_{\alpha\beta} X^{\Gamma}_{\alpha\alpha} (J_3)^{\alpha\beta}_{ij} X^{\Gamma}_{\beta\beta}. \qquad \text{(C12)}$$

At this point, it is important to recall that the sum over Γ in Eq. (C8) [and, obviously, in Eq. (12)] includes an implicit sum over the components of multidimensional representations; in the present case only E is multidimensional. The irreducible coupling constants U^{Γ}_{ij} given by Eq. (C9) are a property of the pairing channel and therefore of the representation. As a result, they must be the same for all components of a representation and are appropriately labeled by Γ. Importantly, however, each of the interaction parameters on the right-hand side of (C9) need *not* be the same for all components of a representation, only their sum. In particular, the expressions of Eqs. (C10)–(C12) should be evaluated for each component of a representation Γ. This fact is obscured by adopting a more compact notation, but the reader is cautioned to keep this in mind.

The requirement that U^{Γ}_{ij} defines the coupling constant of a representation Γ gives rise to a constraint on the interaction parameters V and $J_{1,2,3}$ since their sum must be proportional to the identity within each representation. The consequences of such constraint are exemplified by the onsite Hamiltonian of Eq. (7), which is specified in terms of only two interaction energy scales.

APPENDIX D: FURTHER DECOMPOSITION OF EQ. (20)

The decomposition of $U^{\Gamma}_{\nu\nu'}(\mathbf{k}' - \mathbf{k})$ follows the standard scheme for identifying the irreducible pairing channels in a system with symmetry group $\mathcal{G}$. As explained in Sec. III, the vertex function $U^{\Gamma}_{\nu\nu'}(\mathbf{k})$ is the Fourier transform of the interactions between pairs, which in practice will be short ranged and thus limited to the first few nearest neighbors. Using the notation of Appendix B, the interaction parameters can be denoted U^{Γ}_{γ}, where $\gamma = 1, 2, 3$ corresponds to first-, second-, and third-nearest neighbors; U^{Γ}_0 defines the onsite interactions. As an example, the term in $U^{\Gamma}_{\nu\nu'}(\mathbf{k})$ corresponding to first-nearest-neighbor interactions takes the form

$$U^{\Gamma}_{AB,1}(\mathbf{k}) = U^{\Gamma*}_{BA,1}(\mathbf{k}) = U^{\Gamma}_1 \sum_n \exp(i\mathbf{k} \cdot \mathbf{d}_n), \qquad \text{(D1)}$$

where $\mathbf{d}_{n=1,2,3}$ denote the nearest-neighbor vectors in the direction $\hat{\mathbf{e}}_n$ (see Fig. 4). Similarly, the second-nearest-neighbor interactions are given by

$$U^{\Gamma}_{AA,2}(\mathbf{k}) = U^{\Gamma}_{BB,2}(\mathbf{k}) = U^{\Gamma}_2 \sum_n \cos \mathbf{k} \cdot \mathbf{a}_n, \qquad \text{(D2)}$$

where $\mathbf{a}_{n=1,2,3}$ are the three primitive lattice vectors shown in Fig. 4.

For each γ, the next step is to decompose $U_{\nu\nu'}^{\Gamma}(\mathbf{k})$ into lattice harmonics $f^{\Gamma'}(\mathbf{k})$ as

$$U_{\gamma}^{\Gamma}(\mathbf{k}' - \mathbf{k}) = U_{\gamma}^{\Gamma} \sum_{\Gamma'} f^{\Gamma'*}(\mathbf{k}') f^{\Gamma'}(\mathbf{k}), \qquad (D3)$$

where we have suppressed the sublattice $\nu\nu'$ for simplicity. The sum over Γ' should be understood as a sum over all distinct symmetry quantum numbers, which in particular includes a sum over the components of multidimensional representations. To showcase (D3), consider the second-nearest-neighbor interactions given by (D2). In this case $U_2^{\Gamma}(\mathbf{k}' - \mathbf{k})$ is decomposed into a sum over six lattice harmonics given by

$$f^{A_1,+}(\mathbf{k}) = \sum_n \cos \mathbf{k} \cdot \mathbf{a}_n, \qquad (D4)$$

$$f^{E_1,+}(\mathbf{k}) = \text{Re} \sum_n e^{i4\pi(n-1)/3} \cos \mathbf{k} \cdot \mathbf{a}_n, \qquad (D5)$$

$$f^{E_2,+}(\mathbf{k}) = \text{Im} \sum_n e^{i4\pi(n-1)/3} \cos \mathbf{k} \cdot \mathbf{a}_n, \qquad (D6)$$

as well as $f^{A_1,-}(\mathbf{k})$ and $f^{E,-}(\mathbf{k})$ obtained from (D4)–(D6) by replacing $\cos \mathbf{k} \cdot \mathbf{a}_n$ with $\sin \mathbf{k} \cdot \mathbf{a}_n$. Note that the functions $f^{\pm}(\mathbf{k})$ have the property $f^{\pm}(-\mathbf{k}) = \pm f^{\pm}(\mathbf{k})$. The parity under $\mathbf{k} \to -\mathbf{k}$ is important since Fermi statistics implies

$$\Pi_{\mathbf{k}\Gamma,SM}^{\dagger} = (-1)^{p_{\Gamma}+p_S+1} \Pi_{-\mathbf{k}\Gamma,SM}^{\dagger}. \qquad (D7)$$

The final step is to form irreducible momentum space pairing operators by coupling the lattice harmonics to the orbital degree of freedom. This amounts to taking the product $\Gamma' \otimes \Gamma$, where the first refers to the lattice and second to the orbital degree of freedom, and decomposing it into irreducible terms. This exactly analogous to forming total angular pairing operators in spin-orbit-coupled systems, in which spin is locked to the lattice. Here, instead, the orbital degree of freedom is (intrinsically) locked to the lattice.

APPENDIX E: DECOMPOSITION INTO IRREDUCIBLE PARTICLE-HOLE CHANNELS

The particle-hole pair operators $\Lambda_{i\alpha\sigma,j\beta\sigma'}$ are defined in (28) and their decomposition in terms of orbital and spin symmetrized pair operators is given by Eq. (29). The spin singlet/triplet and the coefficients $C_{\sigma\sigma'}^a$ are given by (suppressing orbital indices)

$$\Lambda_{ij,a} = \sum_{\sigma\sigma'} c_{i\sigma}^{\dagger} s_{\sigma\sigma'}^a c_{j\sigma'}, \quad \widetilde{C}_{\sigma\sigma'}^a = \frac{1}{2} s_{\sigma'\sigma}^a. \qquad (E1)$$

Here, $s^{x,y,z}$ are a set of Pauli matrices acting on the electron spin and s^0 is the identity; recall that $a = 0, x, y, z$. The symmetrized orbital operators are defined as (suppressing spin indices)

$$\Lambda_{ij,A_1} = \sum_{\alpha\beta} \delta_{\alpha\beta} c_{i\alpha}^{\dagger} c_{j\beta}, \quad \Lambda_{ij,A_2} = \sum_{\alpha\beta} c_{i\alpha}^{\dagger} \tau_{\alpha\beta}^y c_{j\beta}, \quad (E2)$$

$$(\Lambda_{ij,E_1}, \Lambda_{ij,E_2}) = \sum_{\alpha\beta} (\tau_{\alpha\beta}^z, \tau_{\alpha\beta}^x) c_{i\alpha}^{\dagger} c_{j\beta}, \qquad (E3)$$

and the orbital expansion coefficients $Y_{\alpha\beta}^{\Gamma}$ are given by

$$Y_{\alpha\beta}^{A_1} = \frac{1}{2} \delta_{\alpha\beta}, \quad Y_{\alpha\beta}^{A_2} = \frac{1}{2} \tau_{\beta\alpha}^y, \qquad (E4)$$

$$(Y_{\alpha\beta}^{E_1}, Y_{\alpha\beta}^{E_2}) = \frac{1}{2} (\tau_{\alpha\beta}^z, \tau_{\alpha\beta}^x). \qquad (E5)$$

With these definitions one has $\Lambda_{ji,\Gamma a} = \Lambda_{ij,\Gamma a}^{\dagger}$, which implies that

$$\Lambda_{ji,\Gamma a} \Lambda_{ij,\Gamma a} = \Lambda_{ij,\Gamma a}^{\dagger} \Lambda_{ij,\Gamma a} = |\Lambda_{ij,\Gamma a}|^2. \qquad (E6)$$

Using the expansion coefficients and Eq. (29), the interaction parameters $\tilde{U}_{1,ij}^{\Gamma a}$ and $\tilde{U}_{2,ij}^{\Gamma a}$ of Eq. (32) can be determined. In contrast to the pairing case, here the interaction parameters depend on the spin structure of the symmetrized particle-hole operators. We must distinguish singlet interactions ($a = 0$) and singlet interactions ($a = x, y, z$). For the case $\tilde{U}_{1,ij}^{\Gamma a}$ we find

$$\tilde{U}_{1,ij}^{\Gamma,0} = \tilde{V}_{1,ij}^{\Gamma} + \tilde{J}_{11,ij}^{\Gamma} + \tilde{J}_{21,ij}^{\Gamma} + \tilde{J}_{31,ij}^{\Gamma}, \qquad (E7)$$

$$\tilde{U}_{1,ij}^{\Gamma x,y,z} = \tilde{J}_{11,ij}^{\Gamma} + \tilde{J}_{21,ij}^{\Gamma} + \tilde{J}_{31,ij}^{\Gamma}, \qquad (E8)$$

whereas for the parameters $\tilde{U}_{2,ij}^{\Gamma a}$ we find

$$\tilde{U}_{2,ij}^{\Gamma 0} = \tilde{V}_{2,ij}^{\Gamma} + \tilde{J}_{12,ij}^{\Gamma} + \tilde{J}_{22,ij}^{\Gamma} + \tilde{J}_{32,ij}^{\Gamma}, \qquad (E9)$$

$$\tilde{U}_{2,ij}^{\Gamma x,y,z} = \tilde{V}_{2,ij}^{\Gamma}. \qquad (E10)$$

The parameters on the right-hand side are given by

$$\tilde{J}_{11,ij}^{\Gamma} = -\frac{1}{2} \sum_{\alpha\beta} Y_{\alpha\beta}^{\Gamma} (J_1)_{ij}^{\alpha\beta} Y_{\beta\alpha}^{\Gamma}, \qquad (E11)$$

$$\tilde{J}_{12,ij}^{\Gamma} = \sum_{\alpha\beta} Y_{\alpha\alpha}^{\Gamma} (J_1)_{ij}^{\alpha\beta} Y_{\beta\beta}^{\Gamma} \qquad (E12)$$

for the J_1 exchange interaction,

$$\tilde{J}_{21,ij}^{\Gamma} = -\frac{1}{2} \sum_{\alpha\beta} Y_{\alpha\alpha}^{\Gamma} (J_2)_{ij}^{\alpha\beta} Y_{\beta\beta}^{\Gamma}, \qquad (E13)$$

$$\tilde{J}_{22,ij}^{\Gamma} = \sum_{\alpha\beta} Y_{\alpha\beta}^{\Gamma} (J_2)_{ij}^{\alpha\beta} Y_{\beta\alpha}^{\Gamma} \qquad (E14)$$

for the J_2 exchange interaction, and

$$\tilde{J}_{31,ij}^{\Gamma} = -\frac{1}{2} \sum_{\alpha\beta} Y_{\alpha\beta}^{\Gamma} (J_3)_{ij}^{\alpha\beta} Y_{\beta\alpha}^{\Gamma}, \qquad (E15)$$

$$\tilde{J}_{32,ij}^{\Gamma} = \sum_{\alpha\beta} Y_{\alpha\beta}^{\Gamma} (J_3)_{ij}^{\alpha\beta} Y_{\alpha\beta}^{\Gamma} \qquad (E16)$$

for the J_3 exchange interaction.

APPENDIX F: ORBITAL τ VARIABLES IN THE CHIRAL BASIS

It is convenient to rearrange the orbital Pauli matrices $\boldsymbol{\tau}_i = (\tau_i^x, \tau_i^y, \tau_i^z)$ in a way which exploits their transformation properties under rotations in orbital space (see also Appendix A). To make this explicit we can relabel the Pauli matrices as

$$\boldsymbol{\tau}_i \to (\tau_i^1, \tau_i^2, \tau_i^3) \equiv (\tau_i^z, \tau_i^x, \tau_i^y). \qquad (F1)$$

In this way, τ^3 generates rotations about the z axis and (τ_i^1, τ_i^2) transform as a nematic director under such rotations. To see this clearly, recall Eqs. (A2) and (A3), which show how τ_i transforms under rotations of the orbitals. In terms of the redefined τ_i variables of (F1) the rotation of τ_i can be expressed in the simple form

$$U_\varphi \tau_i^1 U_\varphi^\dagger = \hat{\mathbf{e}}_{2\varphi} \cdot \boldsymbol{\tau}_i, \quad U_\varphi \tau^2 U_\varphi^\dagger = \hat{\mathbf{e}}_{2\varphi}^\perp \cdot \boldsymbol{\tau}_i, \quad \text{(F2)}$$

where the use of the dot product now has a natural interpretation. Since the orbitals $p_{ix,y}$ are eigenstates of τ_i^1, the rotated orbitals $p'_{ix,y}$ of Eq. (A1) are eigenstates of $\hat{\mathbf{e}}_{2\varphi} \cdot \boldsymbol{\tau}_i$.

As mentioned, the redefinition of (F1) is designed so that τ^3 generates rotations about the z axis. Rotations by π about the x axis are represented by τ^1 and rotations by π about the bisector of the x and y axes are represented by τ^2. This implies that under rotations by π about the x axis, the τ variables change as $\tau^1 \to \tau^1$, $\tau^{2,3} \to -\tau^{2,3}$. Therefore, if we rotate the orbitals by $180°$ about the x axis, which changes (p_x, p_y) to $(p_x, -p_y)$, the Pauli matrices τ^1 and τ^2 transform under rotations by φ as $\tau^1 \to \hat{\mathbf{e}}_{-2\varphi} \cdot \boldsymbol{\tau}$ and $\tau^2 \to \hat{\mathbf{e}}_{-2\varphi}^\perp \cdot \boldsymbol{\tau}$ [79]. This is very useful since $\varphi = -2\varphi$ for $\varphi = 0, 2\pi/3, 4\pi/3$, which are precisely the angles corresponding to the three nearest-neighbor bond directions $\hat{\mathbf{e}}_{n=1,2,3}$ of the honeycomb lattice

(see Fig. 4). As a result, the eigenstates of $\hat{\mathbf{e}}_n \cdot \boldsymbol{\tau}$ are precisely the p'_x and $-p'_y$ orbitals along bond $\hat{\mathbf{e}}_n$.

With the relabeling of $\boldsymbol{\tau}_i$ matrices and the basis transformation of the orbitals it is then a simple matter to construct the orbital projection operators of Eqs. (38) and (39). Note first that

$$\mathcal{P}_i^{x,y} = \tfrac{1}{2}(1 \pm \hat{\mathbf{e}}_{ij} \cdot \boldsymbol{\tau}_i) \quad \text{(F3)}$$

are projection operators which project onto the orbitals $p'_{ix} = (p_{ix}\hat{\mathbf{e}}_x + p_{iy}\hat{\mathbf{e}}_y) \cdot \hat{\mathbf{e}}_{ij}$ and $p'_{iy} = (p_{ix}\hat{\mathbf{e}}_x + p_{iy}\hat{\mathbf{e}}_y) \cdot \hat{\mathbf{e}}_{ij}^\perp$. The same is true for site j: $\mathcal{P}_j^{x,y} = \tfrac{1}{2}(1 \pm \hat{\mathbf{e}}_{ij} \cdot \boldsymbol{\tau}_j)$. From these we define the four projection operators $\mathcal{P}_{ij}^{xx}$, $\mathcal{P}_{ij}^{yy}$, $\mathcal{P}_{ij}^{xy}$, and $\mathcal{P}_{ij}^{yx}$ given by

$$\mathcal{P}_{ij}^{x,y;x,y} = \tfrac{1}{4}(1 \pm \hat{\mathbf{e}}_{ij} \cdot \boldsymbol{\tau}_i)(1 \pm \hat{\mathbf{e}}_{ij} \cdot \boldsymbol{\tau}_j). \quad \text{(F4)}$$

The orbital flip operators of Eqs. (40) and (41) are defined based on the same conventions. In particular, for two nearest-neighbor sites i and j the orbital raising and lowering operators are defined as

$$\tau_i^\pm = \mathbf{e}_{ij}^\perp \cdot \boldsymbol{\tau}_i \pm i\tau_i^3, \quad \tau_j^\pm = \mathbf{e}_{ij}^\perp \cdot \boldsymbol{\tau}_j \pm i\tau_j^3. \quad \text{(F5)}$$

For the case $\mathbf{e}_{ij} = \mathbf{e}_{n=1}$, this reduces to $\tau_i^\pm = \tau_i^2 \pm i\tau_i^3 = \tau_i^x \pm i\tau_i^y$.

[1] Y. Cao, V. Fatemi, A. Demir, S. Fang, S. L. Tomarken, J. Y. Luo, J. D. Sanchez-Yamagishi, K. Watanabe, T. Taniguchi, E. Kaxiras, R. C. Ashoori, and P. Jarillo-Herrero, Nature (London) **556**, 80 (2018).

[2] Y. Cao, V. Fatemi, S. Fang, K. Watanabe, T. Taniguchi, E. Kaxiras, and P. Jarillo-Herrero, Nature (London) **556**, 43 (2018).

[3] E. J. Mele, Nat. News Views **556**, 37 (2018).

[4] C. Xu and L. Balents, Phys. Rev. Lett. **121**, 087001 (2018).

[5] N. F. Q. Yuan and L. Fu, Phys. Rev. B **98**, 045103 (2018).

[6] H. C. Po, L. Zou, A. Vishwanath, and T. Senthil, Phys. Rev. X **8**, 031089 (2018).

[7] B. Roy and V. Juricic, arXiv:1803.11190.

[8] H. Guo, X. Zhu, S. Feng, and R. T. Scalettar, Phys. Rev. B **97**, 235453 (2018).

[9] G. Baskaran, arXiv:1804.00627.

[10] B. Padhi, C. Setty, and P. W. Phillips, Nano Lett. **18**, 6175 (2018).

[11] V. Y. Irkhin and Y. N. Skryabin, Sov. J. Exp. Theor. Phys. Lett. **107**, 651 (2018).

[12] J. F. Dodaro, S. A. Kivelson, Y. Schattner, X.-Q. Sun, and C. Wang, Phys. Rev. B **98**, 075154 (2018).

[13] T. Huang, L. Zhang, and T. Ma, arXiv:1804.06096.

[14] L. Zhang, arXiv:1804.09047.

[15] S. Ray and T. Das, arXiv:1804.09674.

[16] C.-C. Liu, L.-D. Zhang, W.-Q. Chen, and F. Yang, Phys. Rev. Lett. **121**, 217001 (2018).

[17] X. Y. Xu, K. Law, and P. A. Lee, Phys. Rev. B **98**, 121406 (2018).

[18] J. Kang and O. Vafek, Phys. Rev. X **8**, 031088 (2018).

[19] L. Rademaker and P. Mellado, arXiv:1805.05294.

[20] H. Isobe, N. F. Q. Yuan, and L. Fu, arXiv:1805.06449.

[21] M. Koshino, N. F. Q. Yuan, T. Koretsune, M. Ochi, K. Kuroki, and L. Fu, Phys. Rev. X **8**, 031087 (2018).

[22] F. Wu, A. H. MacDonald, and I. Martin, arXiv:1805.08735.

[23] J. M. Pizarro, M. J. Calderón, and E. Bascones, arXiv:1805.07303.

[24] T. J. Peltonen, R. Ojajärvi, and T. T. Heikkilä, arXiv:1805.01039.

[25] Y.-Z. You and A. Vishwanath, arXiv:1805.06867.

[26] X.-C. Wu, K. A. Pawlak, C.-M. Jian, and C. Xu, arXiv:1805.06906.

[27] H. K. Pal, arXiv:1805.08803.

[28] M. Ochi, M. Koshino, and K. Kuroki, Phys. Rev. B **98**, 081102(R) (2018).

[29] M. Fidrysiak, M. Zegrodnik, and J. Spalek, Phys. Rev. B **98**, 085436 (2018).

[30] D. M. Kennes, J. Lischner, and C. Karrasch, arXiv:1805.06310.

[31] A. Thomson, S. Chatterjee, S. Sachdev, and M. S. Scheurer, Phys. Rev. B **98**, 075109 (2018).

[32] F. Guinea and N. R. Walet, arXiv:1806.05990.

[33] H. Patel, L. Huang, C.-J. Kim, J. Park, and M. W. Graham, arXiv:1806.06312.

[34] L. Zou, H. C. Po, A. Vishwanath, and T. Senthil, Phys. Rev. B **98**, 085435 (2018).

[35] J. González and T. Stauber, arXiv:1807.01275.

[36] Y. Su and S.-Z. Lin, Phys. Rev. B **98**, 195101 (2018).

[37] B. Lian, Z. Wang, and B. A. Bernevig, arXiv:1807.04382.

[38] Y. Sherkunov and J. J. Betouras, arXiv:1807.05524.

[39] A. O. Sboychakov, A. V. Rozhkov, A. L. Rakhmanov, and F. Nori, arXiv:1807.08190.

[40] Z. Song, Z. Wang, W. Shi, G. Li, C. Fang, and B. A. Bernevig, arXiv:1807.10676.

[41] B. Lingam Chittari, N. Leconte, S. Javvaji, and J. Jung, arXiv:1808.00104.

[42] K. Hejazi, C. Liu, H. Shapourian, X. Chen, and L. Balents, arXiv:1808.01568.

[43] H. C. Po, L. Zou, A. Vishwanath, and T. Senthil, arXiv:1808.02482.

[44] X. Lin and D. Tománek, Phys. Rev. B **98**, 081410(R) (2018).

[45] E. Laksono, J. Ning Leaw, A. Reaves, M. Singh, X. Wang, S. Adam, and X. Gu, Solid State Commun. **282**, 38 (2018).

[46] G. Tarnopolsky, A. J. Kruchkov, and A. Vishwanath, arXiv:1808.05250.

[47] Y.-P. Lin and R. M. Nandkishore, arXiv:1808.05270.

[48] J. Ahn, S. Park, and B.-J. Yang, arXiv:1808.05375.

[49] J. P. Carbotte, Rev. Mod. Phys. **62**, 1027 (1990).

[50] P. A. Lee, N. Nagaosa, and X.-G. Wen, Rev. Mod. Phys. **78**, 17 (2006).

[51] D. J. Scalapino, Rev. Mod. Phys. **84**, 1383 (2012).

[52] S. Maiti and A. V. Chubukov, in *Lectures on the Physics of Strongly Correlated Systems XVII: Seventeenth Training Course in the Physics of Strongly Correlated Systems*, edited by A. Avella and F. Mancini, AIP Conf. Proc. No. 1550 (AIP, New York, 2013), p. 3.

[53] J. Nilsson, A. H. Castro Neto, F. Guinea, and N. M. R. Peres, Phys. Rev. Lett. **97**, 266801 (2006).

[54] J. Nilsson, A. H. Castro Neto, F. Guinea, and N. M. R. Peres, Phys. Rev. B **78**, 045405 (2008).

[55] E. McCann and M. Koshino, Rep. Prog. Phys. **76**, 056503 (2013).

[56] A. Rozhkov, A. Sboychakov, A. Rakhmanov, and F. Nori, Phys. Rep. **648**, 1 (2016).

[57] M. Yankowitz, S. Chen, H. Polshyn, K. Watanabe, T. Taniguchi, D. Graf, A. F. Young, and C. R. Dean, arXiv:1808.07865.

[58] S. Shallcross, S. Sharma, E. Kandelaki, and O. A. Pankratov, Phys. Rev. B **81**, 165105 (2010).

[59] E. Suárez Morell, J. D. Correa, P. Vargas, M. Pacheco, and Z. Barticevic, Phys. Rev. B **82**, 121407 (2010).

[60] G. Trambly de Laissardière, D. Mayou, and L. Magaud, Nano Lett. **10**, 804 (2010).

[61] J. Jung, A. Raoux, Z. Qiao, and A. H. MacDonald, Phys. Rev. B **89**, 205414 (2014).

[62] S. Fang and E. Kaxiras, Phys. Rev. B **93**, 235153 (2016).

[63] N. N. T. Nam and M. Koshino, Phys. Rev. B **96**, 075311 (2017).

[64] J. M. B. Lopes dos Santos, N. M. R. Peres, and A. H. Castro Neto, Phys. Rev. Lett. **99**, 256802 (2007).

[65] E. J. Mele, Phys. Rev. B **81**, 161405(R) (2010).

[66] E. J. Mele, Phys. Rev. B **84**, 235439 (2011).

[67] R. Bistritzer and A. H. MacDonald, Proc. Natl. Acad. Sci. USA **108**, 12233 (2011).

[68] J. M. B. Lopes dos Santos, N. M. R. Peres, and A. H. Castro Neto, Phys. Rev. B **86**, 155449 (2012).

[69] M. Koshino and P. Moon, J. Phys. Soc. Jpn. **84**, 121001 (2015).

[70] K. I. Kugel and D. I. Khomskii, Zh. Eksp. Teor. Fiz. **64**, 1429 (1973) [Sov. Phys.–JETP **37**, 725 (1973)].

[71] K. I. Kugel and D. I. Khomskii, Usp. Fiz. Nauk **136**, 621 (1982) [Sov. Phys.–Usp. **25**, 231 (1982)].

[72] M. Imada, A. Fujimori, and Y. Tokura, Rev. Mod. Phys. **70**, 1039 (1998).

[73] E. Dagotto, T. Hotta, and A. Moreo, Phys. Rep. **344**, 1 (2001).

[74] E. Dagotto, *Nanoscale Phase Separation and Colossal Magnetoresistance*, Vol. 136 of Springer Series in Solid State Sciences (Springer, Heidelberg, 2003).

[75] S. Maekawa, T. Tohyama, S. E. Barnes, S. Ishihara, W. Koshibae, and G. Khaliullin, *Physics of Transition Metal Oxides*, Vol. 144 of Springer Series in Solid State Sciences (Springer, Heidelberg, 2004).

[76] J. C. Slater and G. F. Koster, Phys. Rev. **94**, 1498 (1954).

[77] This correspondence is only exact when starting from a low-energy continuum, which is the approach taken in Ref. [21]. When the Wannier states are derived from a microscopic tight-binding model for commensurate TBG, as in Ref. [18], there is no exact valley symmetry.

[78] C. Wu, D. Bergman, L. Balents, and S. Das Sarma, Phys. Rev. Lett. **99**, 070401 (2007).

[79] C. Wu, Phys. Rev. Lett. **100**, 200406 (2008).

[80] A. V. Chubukov, M. Khodas, and R. M. Fernandes, Phys. Rev. X **6**, 041045 (2016).

[81] J. Kanamori, Prog. Theor. Phys. **30**, 275 (1963).

[82] Due to the fact that these are onsite pair operators, the normalization differs by a factor $1/\sqrt{2}$ from the definition of the general irreducible pair operators in Eq. (9).

[83] C. Platt, W. Hanke, and R. Thomale, Adv. Phys. **62**, 453 (2013).

[84] M. Sigrist and K. Ueda, Rev. Mod. Phys. **63**, 239 (1991).

[85] L. Fu, Phys. Rev. B **90**, 100509(R) (2014).

[86] J. W. F. Venderbos, V. Kozii, and L. Fu, Phys. Rev. B **94**, 180504(R) (2016)

[87] R. M. Fernandes, P. P. Orth, and J. Schmalian, arXiv:1804.00818.

[88] E. Fradkin, S. A. Kivelson, and J. M. Tranquada, Rev. Mod. Phys. **87**, 457 (2015).

[89] M. Hecker and J. Schmalian, npj Quantum Mater. **3**, 26 (2018).

[90] F. Y. Wu, Rev. Mod. Phys. **54**, 235 (1982).

[91] L. F. Feiner, A. M. Oleś, and J. Zaanen, Phys. Rev. Lett. **78**, 2799 (1997).

[92] A. M. Oleś, L. F. Feiner, and J. Zaanen, Phys. Rev. B **61**, 6257 (2000).

[93] W. M. H. Natori, E. C. Andrade, and R. G. Pereira, Phys. Rev. B **98**, 195113 (2018).